Growth of binary fluid convection: Role of the concentration field

C. Fütterer* and M. Lücke
Institut für Theoretische Physik, Universität des Saarlandes, Postfach 151150, D-66041 Saarbrücken, Germany
(Received 20 June 2001; published 6 March 2002)

The growth of convection in binary fluid mixtures out of different perturbations of the quiescent conductive state is investigated using finite-difference numerical simulations for realistic ethanol-water parameters with strong negative Soret coupling between temperature and concentration fluctuations. Several different analysis tools are used to elucidate the complex spatiotemporal behavior associated with the dramatic concentration redistribution during the transients. It shows first the competition between counterpropagating waves that initially superimpose to form standing wave perturbations. Having reached a critical amplitude an advective breaking of the concentration wave triggers a very fast flow-induced transition from standing to traveling wave convection with large phase velocity and large concentration field amplitudes. Strongly nonlinear advective mixing and weak long-time diffusive homogenization then slow down the waves.

DOI: 10.1103/PhysRevE.65.036315 PACS number(s): 47.20.−k, 47.10.+g, 47.27.Te, 47.54.+r

I. INTRODUCTION

The growth of convection in a shallow layer of room temperature water heated from below changes significantly if one adds, say, 5% of alcohol. In pure water there is the well known smooth (second-order) transition associated with a nonhysteretic forwards bifurcation from the quiescent fluid to stationary, weakly nonlinear convective rolls that are close to the convective onset just a mild perturbation of the quiescent conductive basic state [1,2]. In the aforementioned binary mixture, however, the transition is precipitous (of first order) and, more important, it shows much more dynamical as well as structural complexity. It is associated with a hysteretic backwards bifurcation at an increased heating rate into a large-amplitude, strongly nonlinear oscillatory structure of rolls that either travel to the left or to the right relative to their axes. Moreover, there is a dramatic redistribution of alcohol during this transition that is the key to understanding the convective properties in such a mixture.

It is the concentration field that is responsible for the increase in complexity of binary mixture convection compared to pure fluids and that causes the different spatiotemporal properties of the convective structures, of the bifurcation behavior, and of the transient growth of convection. In the above mentioned example mixture the concentration field is strongly [3] coupled to the temperature field by the Soret effect that causes concentration gradients and currents in linear response to temperature gradients. These Soret generated concentration variations influence the buoyancy, i.e., the driving force for convective flow. The latter in turn advectively redistributes concentration and mixes the two components thereby evening out concentration variations. This nonlinear advective mixing gets in developed convective flow typically much larger than the smoothening by linear diffusion. Thus, the concentration balance is strongly nonlinear giving rise to boundary layer behavior, among others, while the momentum and heat balances remain weakly nonlinear close to onset as in pure fluids. To summarize, the feedback interplay between (i) the Soret generated concentration variations that are sustained against mixing and diffusion by externally imposed and internal temperature gradients, (ii) the resulting changes in the buoyancy, (iii) the strongly nonlinear advective transport and mixing, and (iv) the smoothening dissipative solutal diffusion causes the larger spatiotemporal complexity of binary mixture convection.

The latter has been the subject of many studies [4]. Being too numerous to be discussed here we pick out some of those that address the special role of the concentration field. The buoyancy difference in regions with different concentrations was identified already in Ref. [5] as the cause for traveling wave (TW) convection. With increasing heating, i.e., with increasing flow the mixing increases and the concentration variations decrease. This causes a characteristic decrease of the TW frequency ω. Measurements of the variation of ω with Rayleigh number were shown [6,7] to agree with numerical calculations [8]. The concentration-boundary-layer model of Bensimon *et al.* [9] showed the same characteristic decrease of ω near the end of the TW bifurcation branch. For large flow concentration becomes trapped in regions of closed streamlines where it gets diffusively homogenized [8,10] like a weakly diffusing passive scalar for large Péclet numbers [11]. This effect is one part of the explanation [10,12,13] that the lateral concentration profile of a TW is trapezoidal with constant, i.e., diffusively smoothened plateaus in the central roll regions and linear variation between adjacent rolls. Since the latter are fed alternatingly by the top and bottom boundary layers containing concentration at different levels [10,12,13] the aforementioned plateaus are at alternatingly high and low concentration levels. These co5ncentration variations modify the refractive index of the mixture and thus cause characteristic variations of shadowgraph images. Comparing topview images of TW states [14] with numerical results [15] allowed to identify the characteristic contribution from the concentration field. This seems to have been the first time that structural properties of the concentration field—albeit vertically averaged—in binary fluid convection have been observed experimentally. Subsequently, Winkler and Kolodner [16] extracted more direct information

*Present address: Institut Curie PCC, 11 rue P. et M. Curie, F-75005 Paris, France

on the lateral structure of the concentration distribution in TWs from sideview shadowgraph images obtaining good agreement with numerical results [15].

The time series of sideview shadowgraph images shown in Ref. [16] after increasing the Rayleigh number beyond the convective threshold gave also information about the transient spatiotemporal evolution of the concentration field in growing convection and, in particular, about the formation of boundary layers. Also the Lagrangian dynamics of advection and diffusion of passive fluorescent dye particles that were photochromically marked in a small spatial region of exponentially growing linear TWs and of nonlinear relaxed TWs was visualized [17]. Besides that there have been many experimental investigations of transient convection phenomena [7,18–26]. But, unfortunately, the resolutions of the topview shadowgraphs were not layed out to measure also the concentration dynamics during the transient growth processes of weakly nonlinear TWs and of linear TW packets [18], of weakly nonlinear counterpropagating TWs [19] that are reflected from endwalls of rectangular channels, of ''blinking states'' [19,22] with TW amplitude becoming alternatingly large at the sidewalls before being reflected with reduced amplitude, of the ''dispersive chaos'' [24] produced by erratic burst and decay of TW pulses, and of TW patches in large cylindrical [23,25] or otherwise shaped containers [26].

On the other hand, numerical simulations [10,27–31] gave indications that the concentration field is spatiotemporally quite complex and plays a decisive role in the (transient growth) behavior of convection. This has to be contrasted with weakly nonlinear analytical analyses in the framework of amplitude equations [32,33]. Therein the concentration field is enforced by the construction of this approximation to show the same spatiotemporal behavior as those of velocity and temperature since all of them are described on equal footing by just one common amplitude of a laterally and temporally harmonic wave [34].

In this paper we elucidate that the transient growth of binary mixture convection implies a dramatic concentration redistribution that causes a very special change in the spatiotemporal behavior. Stepping up the heating across the critical threshold one finds initially the conductive state's horizontal concentration stratification with a large Soret generated vertical gradient. Generic perturbations of this state trigger then growth of the two critical TW modes. Their amplitudes being typically of roughly the same size these linear counterpropagating TWs superimpose to a standing wave (SW) that oscillates with the large Hopf frequency ω_H while growing in amplitude. Reaching a critical amplitude the concentration wave topples and breaks in a very fast advection driven process. The crests and troughs get rolled in and the SW is transformed advectively into a pure, large-amplitude TW. The latter has initially a lateral concentration contrast that is almost as large as the vertical one of the conductive state and consequently its frequency ω is still almost as large as ω_H. But then diffusive homogenization causes a long-time smoothening and decrease of TW frequency and a slow relaxation into a final, well mixed, low-frequency, strongly nonlinear TW.

We provide a detailed numerical investigation of this and other related transition scenarios using various analysis tools. Calculations are done in a (2D) two-dimensional vertical cross section of the fluid layer with laterally periodic boundary conditions. The periodicity length of twice the layer thickness is close to the critical wavelength of roll perturbations and also close to typical (local) values observed in convection experiments. However, imposing the periodicity length of one wavelength precludes some of the instabilities of large systems and the complex spatial structures found in 3D experimental setups [25,31,35–37].

Our paper is organized as follows: In Sec. II we describe the system and in Sec. III we give a brief summary of the properties of nonlinear, fully relaxed TW convection before presenting in Sec. IV our results on the transient growth out of different types of perturbations of the quiescent conductive state. The last section contains a summary of the main results.

II. SYSTEM

We consider a binary fluid layer of mean temperature $\overline{T}$ and mean concentration $\overline{C}$ of the lighter component (e.g., ethanol). It is confined between two perfectly heat conducting, impervious, horizontal plates and exposed to a vertical gravitational acceleration g and to a vertical temperature gradient $\Delta T/d$ directed from top to bottom where d is the layer thickness. The variation of the fluid density ρ due to temperature and concentration variations is governed by the linear thermal and solutal expansion coefficients $\alpha=-(1/\rho)(\partial\rho/\partial\overline{T})$ and $\beta=-(1/\rho)(\partial\rho/\partial\overline{C})$, respectively. Both are positive for ethanol water. The solutal diffusivity of the binary mixture is D, its thermal diffusivity is κ, and its viscosity is ν. The thermodiffusion coefficient k_T [38] quantifies the Soret coupling that describes the change of concentration fluctuations due to temperature gradients in the fluid.

The vertical thermal diffusion time is used as the time scale d^2/κ of the system and all velocities are scaled by κ/d. Temperatures are reduced by the vertical temperature difference ΔT across the layer and concentration deviations from the mean concentration by $(\alpha/\beta)\Delta T$. The scale for the pressure is given by $(\rho\kappa^2/d^2)$. Then, the balance equations for mass, momentum, heat, and concentration [38,39] read in Oberbeck–Boussinesq approximation [13],

$$0=-\boldsymbol{\nabla}\cdot\mathbf{u}, \tag{2.1a}$$

$$\partial_t\mathbf{u}=-(\mathbf{u}\cdot\boldsymbol{\nabla})\mathbf{u}-\boldsymbol{\nabla}\left[p+\left(\frac{d^3}{\kappa^2}g\right)z\right]+\sigma\nabla^2\mathbf{u}+R\sigma(T+C)\mathbf{e}_z, \tag{2.1b}$$

$$\partial_t T=-\boldsymbol{\nabla}\cdot\mathbf{Q}=-\boldsymbol{\nabla}\cdot[\mathbf{u}T-\boldsymbol{\nabla}T], \tag{2.1c}$$

$$\partial_t C=-\boldsymbol{\nabla}\cdot\mathbf{J}=-\boldsymbol{\nabla}\cdot[\mathbf{u}C-L\boldsymbol{\nabla}(C-\psi T)]. \tag{2.1d}$$

Here, T and C denote deviations of the temperature and concentration fields, respectively, from their global mean values $\overline{T}$ and $\overline{C}$ and $\mathbf{Q}$ and $\mathbf{J}$ are the associated currents. The Dufour effect [40,41] that provides a coupling of concentration gra-

dients into the heat current **Q** and a change of the thermal diffusivity is discarded in Eq. (2.1c) since it is relevant only in few binary gas mixtures [42] and possibly in liquids near the liquid–vapor critical point [43].

Besides the Rayleigh number $R=(\alpha g d^3/\nu\kappa)\Delta T$ measuring the thermal driving of the fluid three additional numbers enter into the field equations (2.1): the Prandtl number $\sigma=\nu/\kappa$, the Lewis number $L=D/\kappa$, and the separation ratio $\psi=-(\beta/\alpha)(k_T/\overline{T})$. The latter characterizes the sign and the strength of the Soret effect. Negative Soret coupling ψ, as is always assumed here, induces concentration gradients of the lighter component that are antiparallel to temperature gradients. In this situation, the buoyancy induced by solutal changes in density is opposed to the thermal buoyancy. Throughout this paper we consider mixtures with $L=0.01$, $\sigma=10$, and $\psi=-0.25$ being parameters that are easily accessible with ethanol-water experiments.

When the total buoyancy exceeds a threshold, convection sets in—typically in the form of straight rolls for negative ψ. Ignoring field variations along the roll axes we describe here 2D convection in an x-z plane perpendicular to the roll axes with a velocity field,

$$\mathbf{u}(x,z,t)=u(x,z,t)\mathbf{e}_x+w(x,z,t)\mathbf{e}_z. \tag{2.2}$$

This 2D type of convection is commonly enforced experimentally in convection channels of small extension in y direction since the rolls are oriented preferentially perpendicular to the channel walls [2].

To find the time-dependent solutions of the partial differential equations (2.1) describing convection we performed numerical simulations with a modification of the SOLA code that is based on the MAC method [44,45]. This is a finite-difference method of second order in space formulated on staggered grids for the different fields. An explicit first-order Euler step in time was used and the Poisson equation for the pressure field that results from taking the divergence of (2.1b) was solved iteratively using the artificial viscosity method [45]. The boundary conditions for the fields were as follows: we used realistic no slip conditions for the top and bottom plates at $z=\pm 1/2$, i.e.,

$$\mathbf{u}(x,z=\pm 1/2;t)=\mathbf{0}, \tag{2.3a}$$

and we assumed perfect heat conducting plates connected to two heat reservoirs,

$$T(x,z=\pm 1/2;t)=\mp 1/2. \tag{2.3b}$$

Furthermore, impermeability of the horizontal boundaries for the concentration was guaranteed by enforcing the vertical concentration current $\mathbf{e}_z\cdot\mathbf{J}$ to vanish at both plates,

$$\mathbf{e}_z\cdot\mathbf{J}=-L\partial_z(C-\psi T)(x,z=\pm 1/2;t)=0. \tag{2.3c}$$

Restricting our investigation to spatially periodic *extended* convection structures we imposed lateral perodicity in x direction of periodicity length $\lambda=2\pi/k=2$. The associated wave number $k=\pi$ is typically seen in convection experiments done in narrow channels and, furthermore, it is close to the critical wave number for the negative Soret coupling investigated here.

To measure the strength of the thermal driving we use the reduced Rayleigh number $r=R/R_c^0$ that is scaled by the critical Rayleigh number R_c^0 for onset of pure-fluid convection with the critical wave number k_c^0. The analytical values are $R_c^0=1707.762$ and $k_c^0=3.116\,32$. However, to compare our finite differences numerical results presented in this paper with experimental, analytical, or numerical ones we scale R by the threshold R_c^0 of our numerical code. The latter was generally run with uniform spatial resolution of $\Delta=1/20$ for which $R_c^0=1685.8$ [46]. Test runs with $\Delta=1/40$ showed no relevant differences of the transient dynamics.

In order to characterize the temporal evolution of convection we made extensive lateral Fourier analyses of the velocity, temperature, and concentration fields and we determined various spatial profiles of these fields. In addition topview shadowgraph intensity distributions—as they would be seen in experiments—were evaluated from the temperature and concentration fields. Furthermore, we monitored the evolution of the spatial maximum of the vertical velocity field $w_{\max}$, of the oscillation frequency, and of the reduced variance

$$M=\sqrt{\langle C^2\rangle/\langle C_{\mathrm{cond}}^2\rangle} \tag{2.4}$$

of the concentration field. Note that $0\leqslant M\leqslant 1$ measures to which extent the binary fluid is mixed. The better it is mixed the smaller is the spatial mean $\langle C^2\rangle$ of the square of the concentration deviation C from its mean. The boundary condition, however, sustains always small Soret-induced concentration gradients against the action of advection and diffusion and prevents M from vanishing completely. On the other hand, in the conductive state (denoted by the subscript ''cond'') with a Soret-induced vertical concentration stratification given by $C_{\mathrm{cond}}(z)=-\psi z$, there is no advective mixing. Its concentration variance, $\langle C_{\mathrm{cond}}^2\rangle=\psi^2/12$, is largest yielding $M_{\mathrm{cond}}=1$ and at the cold top (warm bottom) plate there is a surplus (deficiency) of magnitude 0.125 (-0.125) when $\psi=-0.25$ as in our case.

III. RELAXED TW CONVECTION

In this section we briefly review properties of the TW and of the stationary overturning convection (SOC) state that are discussed at length in the literature, see, e.g., [13,10,47]. To that end we show in Fig. 1 with thick lines the bifurcation diagrams of maximal vertical flow velocity w_{max}, TW frequency ω, and mixing number M vs reduced Rayleigh number r.

A pair of symmetry degenerate left and right traveling convection wave solutions with wave number $k=\pi$ branch at $r_{osc}=1.337$ out of the conductive state. At this Rayleigh number the system shows a subcritical Hopf bifurcation with a Hopf frequency $\omega_H(k=\pi,r_{osc})=11.233$. Here two facts are worth mentioning: (i) the bifurcation threshold and the

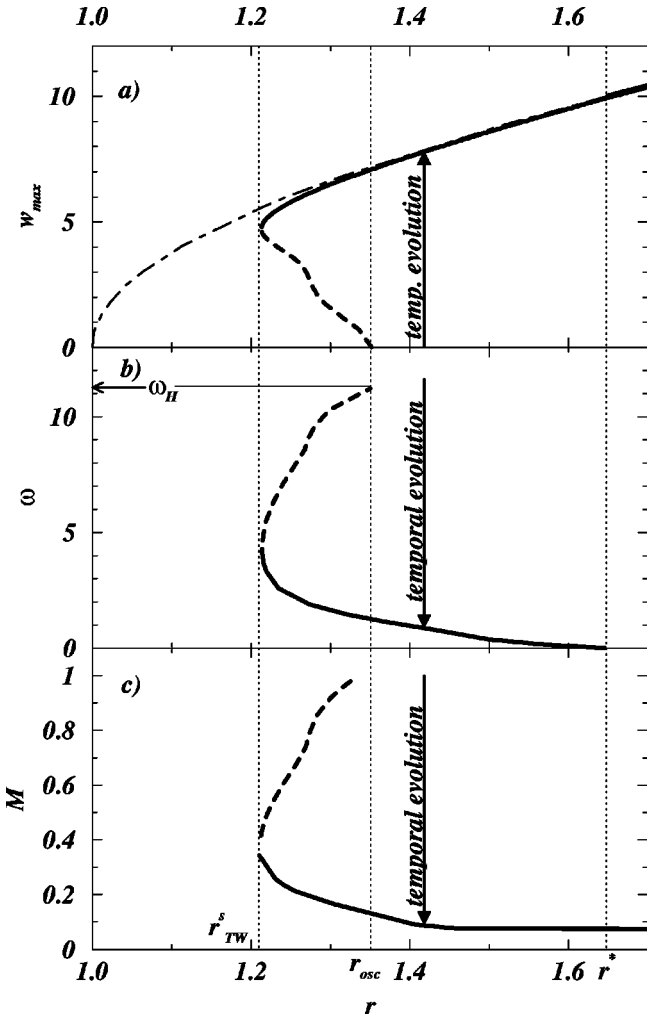

FIG. 1. Bifurcation diagrams of maximal vertical flow velocity w_{max} (a), TW frequency ω (b), and mixing number M (c) vs r for relaxed nonlinear convective states with wavelength $\lambda=2$. Parameters are $L=0.01, \sigma=10, \psi=-0.25$. Full (dashed) thick lines refer to stable (unstable) states. The TW solution bifurcates subcritically with the Hopf frequency ω_H at r_{osc} out of the conductive state, becomes stable at the saddle r^s_{TW}, and ends with zero frequency at r^* on the SOC branch. The dash-dotted line in (a) refers to stationary convection in pure fluids ($\psi=0$). Vertical arrows indicate the time evolution of w_{max}, ω, and M after perturbing the quiescent conductive state. All quantities are reduced ones (cf. Sec. II).

frequency are practically the same as for waves with the critical wave number $k_c=3.1350$ and (ii) TWs with wavelength $\lambda\simeq 2$ are often observed in large-scale experimental setups.

The TW solutions in Fig. 1 become stable at the saddle $r^s_{TW}=1.213$ and they end for the selected parameters at $r^*=1.65$ by merging with vanishing frequency with the SOC solution branch. This point, namely r^*, marks the location of a drift instability of the SOC solution: for $r<r^*$ stationary rolls start to propagate and evolve into a TW solution while for $r>r^*$ the SOC solution is stable. When the Soret coupling ψ becomes more negative r^* increases and eventually seems to diverge so that then the SOC solution remains unstable [13,48].

A. Generation, advective mixing, and diffusion of concentration fluctuations

As the convective flow velocity w_{max} increases along the TW solution branch (Fig. 1) the TW frequency ω and the phase velocity $v=\omega/k$, respectively, decrease monotonically from the large Hopf value all the way to zero since with stronger convection the Soret generated concentration gradients become advectively reduced. Thus, there is a strong correspondence between mixing number M and TW frequency ω [10,48]. In particular, on the stable part (full lines in Fig. 1) of the TW solution branch the binary fluid gets with increasing w_{max} and thermal driving r more and more mixed as M reduces almost to zero. Since the well mixed SOC state resembles closely the corresponding stationary state in the pure fluid with the same σ the bifurcation diagrams of, say, w_{max} or of the Nusselt number in binary mixtures hardly differ at large r from the $\psi=0$ solution in the pure fluid [dash-dotted line in Fig. 1(a)].

The transition to convection at r_{osc} is hysteretic, i.e., of first order with the Soret coupling coefficient $\psi=-0.25$ being sufficiently negative. The associated precipitous growth of convection is related to an interplay between the Soret-induced solutal contribution to the buoyancy [10,13] that tends to stabilize the conductive state and the effect of advective mixing. The latter enhances convection by reducing the adverse effect of the Soret generated concentration variations. The ''*S*''-shaped deformation of the unstable part (dashed lines in Fig. 1) of the TW bifurcation branches occurs when the advection velocity w_{max} has grown to become equal to the TW phase velocity, $v=\omega/\pi$. Then the first closed streamlines appear [47] in the frame of reference that is comoving with the TW phase velocity and in which the TW solution is time independent. For $w_{max}<|v|$, i.e., closer to the threshold r_{osc} all streamlines are open. The condition $w_{max}\simeq|v|$ marks also the threshold beyond which a straightforward small-amplitude expansion around the convective onset breaks down [48]. In addition we found that the generic *transient growth* dynamics of oscillatory convection (consisting initially of oppositely traveling waves of roughly equal velocity amplitudes $|A_R|\simeq|A_L|$) undergoes a dramatic change that cannot be described at all within an amplitude equation picture when the amplitudes $|A_{R,L}|$ approach ω/π.

For $0<|v|<w_{max}$ the open streamlines of relaxed TWs meander between and around the roll-like regions of closed streamlines (in SOC with $v=0$ the only open streamlines are the vertical separation lines between the rolls). In a right-propagating TW the regions of closed streamlines for the right (left) turning fluid domains are rich (poor) in the lighter component—here ethanol—and they are displaced towards the upper cold (lower warm) plate, where the Soret effect has caused a boundary layer with alcohol surplus (deficiency). The open streamlines are such that the top (bottom) boundary layer feeds high (low) concentration only into the right (left) turning roll domain at the location of downflow (upflow). Within the regions of closed streamlines the fluid is trapped and diffusively homogenized leading to anharmonic concentration wave profiles of trapezoidal shape. With increasing w_{max} and decreasing $|v|$ the regions of closed

streamlines grow, the asymmetry of the boundary layer feeding into oppositely turning rolls decreases and with it the concentration contrast between adjacent TW rolls until in the SOC state with $v=0$ mirror symmetry between the rolls is established.

B. Mirror-glide symmetry

All TWs and SOCs discussed in this paper show the mirror-glide (MG) symmetry [8],

$$F(x,z;t)=-F(x+\lambda/2,-z;t), \tag{3.1}$$

with $F(x,z;t)$ denoting ϕ, T, or C. Here ϕ is the stream function defined by $\mathbf{u}(x,z,t)=(-\partial_z\phi,0,\partial_x\phi)$. We should like to stress that also all transients investigated here obeyed the MG symmetry with the exception of the very early stage in cases where the imposed initial conditions were not MG symmetric. But even in such a situation the MG symmetry was rapidly restored by a fast decay of MG symmetry-breaking modes. Also the transient growth seen in the experiments in an annular geometry by Winkler and Kolodner [16] was locally MG symmetric. A time-dependent generalization of this symmetry was found to be realized in spatially localized TW states [49] and an extension to 3D patterns was observed in Ref. [50]. Furthermore, MG symmetric convective structures were not only observed in Soret driven convection with only temperature gradients imposed but also in thermosolutal convection [51].

Thus, the MG symmetry that is displayed by the basic conductive state and the linear critical convective modes seems to be quite robust and persistent also in nonlinear convective structures of pure fluids and of mixtures. The robustness of this symmetry is remarkable given that the nonlinearity in the concentration balance, i.e., the Péclet number w/L is quite large—of the order of 1000. So one might already expect a bifurcation that involves undamped MG symmetry-breaking concentration modes being driven nonlinearly by interactions with MG symmetric modes [52]. However, the concentration field is ''tamed'' by being coupled to the velocity and temperature fields. Their shape remains mostly harmonic in the investigated r range of small supercritical thermal driving such as in pure fluid convection. And thus the increase in structural complexity associated with a MG symmetry breaking does not occur.

IV. TRANSIENT GROWTH

In this section we elucidate the spatiotemporal behavior of the transition from the quiescent ground state being perturbed by different types of perturbations to fully relaxed nonlinear convection.

A. Generic transition behavior; an overview

We start from the ground state at $r<r_{osc}$, disturb it slightly by adding random numbers in the range of $[-10^{-4},10^{-4}]$, and simultaneously increase the control parameter to $r=1.42$ that is 6% above threshold. Unless the initial perturbation is chosen to be very specific one then observes a *generic* transition scenario. The specific dependence on initial conditions is discussed later on in Sec. IV D including *special* cases where, e.g., the initial perturbation consists *precisely* of a critical TW mode or of two different ones with equal amplitudes. The generic growth behavior successively displays evolution phases with different spatiotemporal character. Figures 2 and 3 give an overview of this growth scenario.

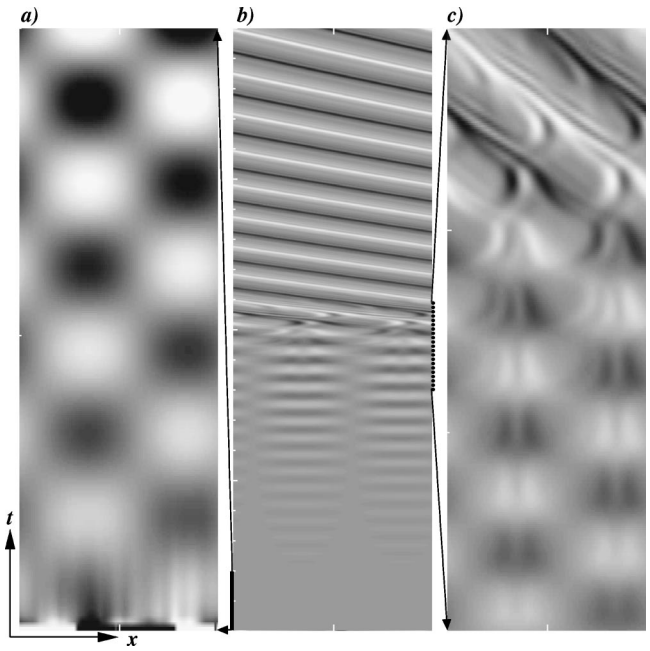

FIG. 2. Time evolution of the topview shadowgraph intensity (4.1) along a line extending laterally over one wavelength after perturbing the quiescent conductive state. The middle part (b) covers the time interval (0, 20) with white tics at the left ordinate of (b) marking one time unit. The left part (a) shows a blow up of the initial time interval (0, 2) of (b) with SW dynamics. The right part (c) shows a blow up of the interval (8, 11) of (b) where the SW transforms into a left-propagating TW. Beyond $t\simeq 11$ this TW slows down. Parameters are $L=0.01$, $\sigma=10$, $\psi=-0.25$, $r=1.42$, and $\lambda=2$.

In Fig. 2 we show the time evolution of the topview shadowgraph intensity [53,14],

$$I(x,t)\sim\partial_x^2\int_{-1/2}^{1/2}\mathrm{d}z[T(x,z,t)-0.919C(x,z,t)] \tag{4.1}$$

as it would be observed in experiments. It is given by the weighted sum of the lateral curvatures of the temperature and of the concentration field. Thus, when the latter develops strong nonharmonic lateral variations with large, spatially confined curvatures then the gray-scale coded intensity distribution in Fig. 2 becomes spiky.

The middle part (b) of this figure covering 20 vertical thermal diffusion times displays the three evolution phases that we have found to be generic for convective growth out of small unspecific perturbations: (*i*) an exponentially growing SW of high frequency over a time interval the length of which depends on the size of the initial perturbations of the

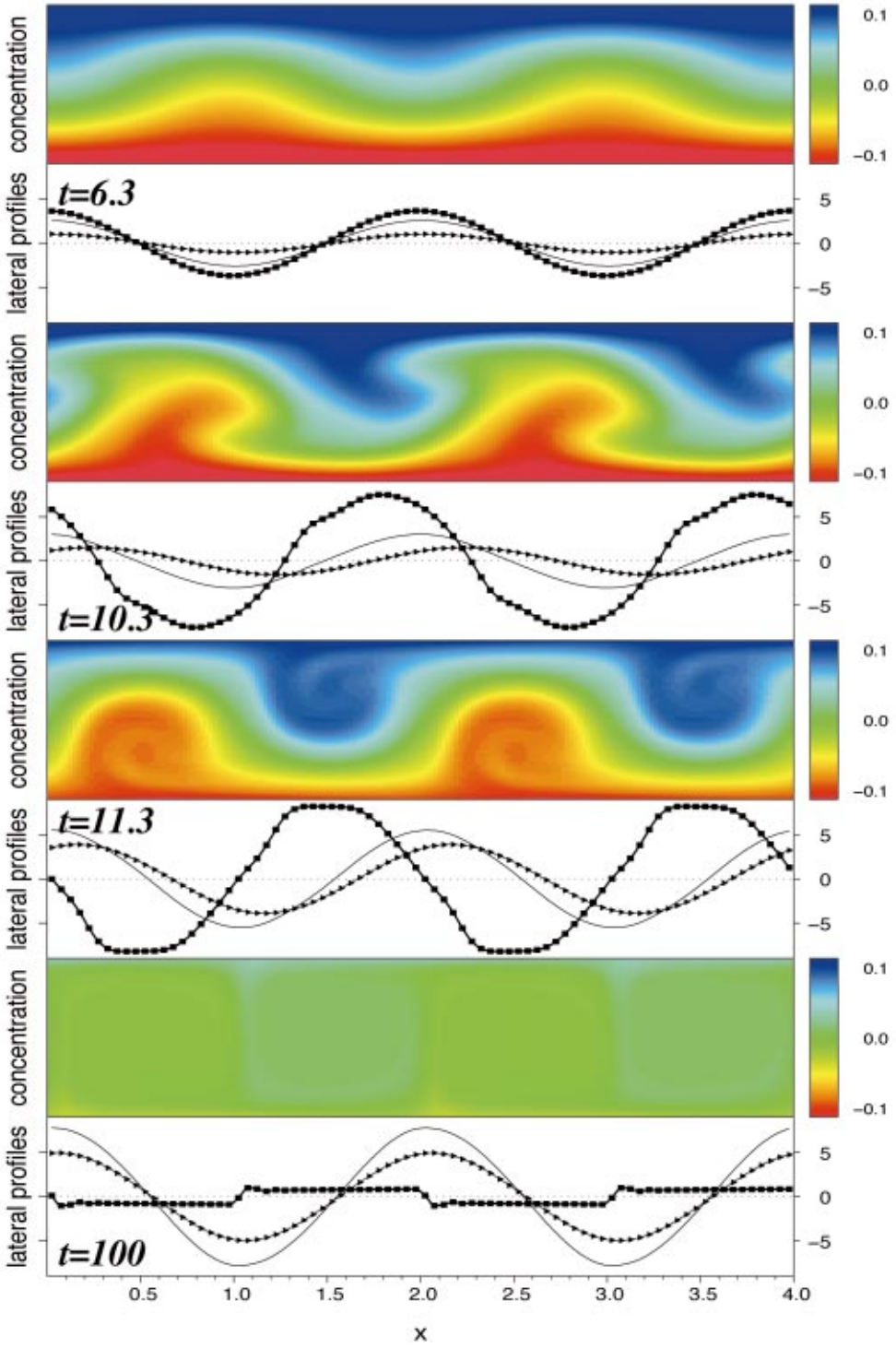

FIG. 3. (Color) Snapshots of the evolution of convection after perturbing the quiescent conductive state. For better visibility two wavelengths are shown. The concentration distribution in a vertical cross section of the fluid layer is displayed by color coded plots with blue and red denoting high and low concentration, respectively. Wave profiles at midheight are shown for the fields of vertical velocity w (thin lines), $40T$ (lines with triangles), and $400C$ (lines with squares). The final TW propagates to the left. All quantities are reduced ones (cf. Sec. II). Parameters are $L=0.01$, $\sigma=10$, $\psi=-0.25$, $r=1.42$, and $\lambda=2$.

conductive state, (*ii*) an intermediate phase that is always very short with a spatiotemporally complicated transformation from SW into a high-frequency TW that is propagating to the left in Figs. 2(b) and 3, and finally (*iii*) a long-term TW transient to a low-frequency, strongly nonlinear, relaxed TW state (head of the vertical arrows in Fig. 1).

Figure 2(a) shows a magnification of the first two diffusion times after perturbing the conductive state with small-amplitude noise. The latter contains besides a narrow band of growing modes with wave number $k=\pi$ and near-critical z

dependence also a multitude of other modes that have larger k and/or noncritical z dependence and that decay under the *linear* initial dynamics. The surviving and exponentially growing modes *generically* superimpose to form a SW—which can be seen in Fig. 2(a) already at time $t \simeq 1/4$—since generic initial perturbations contain the critical eigenmodes of left- and right-propagating TWs with roughly equal amplitude. Thus, this SW shows initially the very smooth, laterally harmonic variation of the critical modes.

In Fig. 2(c) the intermediate interaction phase (*ii*) is shown in detail during the time interval $8<t<11$. At the beginning of this interval [bottom of Fig. 2(c)] the concentration field has already developed a sizeable lateral anharmonicity that subsequently becomes increasingly stronger resulting in a shadowgraph intensity distribution becoming sharper [cf. the time evolution of the stripes in Fig. 2(b) and (c)]. At $t \simeq 10.5$ the convection pattern almost instantly starts to propagate to the left. However, there is also transient motion of some stuctural details to the right to be seen in Fig. 2(c) for a short time interval. This backwards motion is related to the toppling and breaking of the concentration wave that occurs during the SW$\rightarrow$TW transition and that is described in more detail in Sec. IV C. The lateral variation of the shadowgraph intensity of this TW is to an ever increasing extent dominated by the growth in anharmonicity of the concentration wave profile whereas the temperature wave remains harmonic [16]. Hence the TW stripes in the top part of Fig. 2(b) become concentration field dominated and, therefore, sharper. Note that simultaneously their slope increases in the space-time plot of Fig. 2(b) indicating that the TW slows down.

The spatiotemporal evolution of the various fields can be seen in more detail in Fig. 3. Therein we show sideview snapshots of the full concentration field—being the most important one for understanding the transient growth behavior—in a vertical cross section of the fluid layer together with lateral wave profiles of all fields at midheight of the layer. The selected four snapshot times $t=6.3$, 10.3, 11.3, and 100 are characteristic for the different evolutionary phases.

At $t=6.3$ each of the convective fields $F=w,C,T$ still has the form $F \simeq \cos(\omega_0 t+\varphi_F)\cos(kx)$ of an exponentially growing linear SW being mirror symmetric under $x \rightarrow -x$. The oscillation frequency $\omega_0 \simeq 11.51$ is still very close to the fast Hopf frequency that follows from a linear stability analysis of the conductive state for $k=\pi$ at $r=1.42$. The *spatial* location of the nodes of these three fields coincide and lie on vertical straight lines in a genuine linear SW. However, the temporal phases $\varphi_F(z)$ of the critical SW fields vary with z and, moreover, are different for w,C,T. Thus, in a linear SW these fields pass through zero at different times depending on z [32]. At midheight of the layer one has $\varphi_C-\varphi_w \simeq \pi/2$ and $\varphi_T-\varphi_w \simeq -0.17\pi$ [54] for the parameters of Fig. 3.

To discuss the transition from the SW to the TW we decompose the linear spatiotemporal structure of the initial growth phase (*i*) as a superposition of two counterpropagating TWs,

$$F(x,z,t) \sim (1+\eta)\mathcal{T}W_R(x,z,t)+(1-\eta)\mathcal{T}W_L(x,z,t). \tag{4.2}$$

Here $\mathcal{T}W_R$ and $\mathcal{T}W_L$ represent the critical modes for a TW propagating to the right and left, respectively, being mirror images of each other under $x \rightarrow -x$. The asymmetry factor

$$\eta = \frac{|A_R|-|A_L|}{|A_R|+|A_L|} \tag{4.3}$$

in Eq. (4.2) is defined in terms of the amplitudes A_R and A_L of the right and left propagating waves, respectively, such that $\eta=0$ denotes a perfectly mirror-symmetric SW and $\eta=\pm 1$ pure TWs. In fact at $t=6.3$ we found $\eta \simeq -0.01$ so that the SW is not a pure one, but the resulting asymmetry is hardly visible.

By the time $t=10.3$ the concentration wave has become nonlinear with a deformed lateral profile while velocity and temperature waves remain practically harmonic. However, the profiles show now large spatial phase shifts between all fields. Here the C wave is undergoing a complicated transformation (cf. Secs. IV B and IV C for more details) to a TW. The transformation is triggered by a wave breaking and wave toppling process of the crests and troughs of the concentration wave whereas the waves of w and T do not undergo substantial structural changes. In this process the $x \rightarrow -x$ mirror symmetry of the SW gets visibly broken while the MG symmetry (3.1) remains intact throughout this complicated transformation.

In the short interval of one diffusion time to the next snapshot of Fig. 3 at $t=11.3$ the transformation from a high-frequency SW to a high-frequency TW with large C wave amplitudes takes place: the wave crests (troughs) with high (low) content of the lighter component bend and topple in Fig. 3 to the right and are advectively ''rolled in'' in the breaking process of the C wave. They thereby form plateau-like regions of alternatingly high and low concentration in the resulting propagating C-wave. The contrast between the plateaus is at $t=11.3$ almost as large as the initial vertical conductive concentration difference between top and bottom of the fluid layer. This initially large vertical concentration stratification is almost preserved up to this time during the relative short SW transient. Therein the horizontal isoconcentration lines of the conductive state are only swinging up and down with growing amplitude. But then, when the SW amplitude reaches a critical size the wave breaks and thereby the isoconcentration lines are rolled in. This critical size is reached when the velocity field amplitudes, $|A_R|$ and $|A_L|$, of the two TW contributions to the SW have grown roughly to about the phase velocity $v=\omega/\pi$. Note that for ''stationary'' TW solutions the condition of equal flow and phase velocity marks the appearence of (i) closed streamlines in the comoving frame of reference and (ii) of significant nonlinearities as discussed in Sec. III A.

In a sense the vertical concentration contrast of the conductive state has transformed at $t=11.3$ into a lateral one that forms just after the breaking process. With the lateral concentration difference between adjacent roll-like regions still being very large also the frequency of this TW is not

much smaller than ω_0. The phase difference $\varphi_C - \varphi_w$ is still about $\pi/2$ as in the initial SW. However, while being purely temporal in the SW it now implies in the TW also a *spatial* shift of about $\lambda/4$ between the nodes of the traveling C and w waves.

On the long-time scale up to the last snapshot in Fig. 3 at $t = 100$ the large lateral and vertical concentration contrasts of the TW at $t = 11.3$ are degraded diffusively: the spatial extension of the plateaus over which C is constant at the two alternating high and low levels increases, the plateau height decreases, the width of boundary layers between these plateaus shrinks, and the surplus of the lighter (heavier) component in the cold top (warm bottom) part of the fluid layer decreases thus reducing the overall vertical concentration difference between top and bottom. Note that in Fig. 3 the colors blue and red that represent surplus and deficiency, respectively, of the lighter component, e.g., alcohol, have practically disappeared in the final TW plot at $t = 100$ and the color green representing the mean concentration prevails. This long-time degradation of concentration gradients is reflected by a reduction of the mixing number M [Eq. (2.4)] and with it of the frequency ω by a factor of 10 relative to the initial values. Associated with the decrease in ω is also a decrease in the phase shift between the velocity and the temperature waves [55]. In the relaxed final state TW the fluid is well mixed and M and ω are small but still finite.

This slowly propagating TW develops small concentration spikes in the lateral wave profile that precede its plateau regions. The spikes are caused by concentration plumes that alternatingly emanate from the horizontal boundary layers. In these plumes or jets high (low) concentration fluid is advectively transported downwards (upwards) from the top (bottom) boundary layer into the regions of left (right) turning rolls in a TW that is propagating to the left. Within the rolls—or, more precisely, within the regions of closed streamlines in a frame that is comoving with the TW—the plumes advectively spiral inwards and simultaneously are diffusively smoothed out and degraded [13,10,47].

B. Dynamics in Fourier space

To elucidate the spatiotemporal complexity of the transient growth behavior we have also studied lateral Fourier decompositions of all fields at several vertical positions. Here we restrict our discussion to the midheight position, $z = 0$. The behavior of the fields there is representative for all other z, as can also be seen in Fig. 3. A further reduction in the description results from the fact that often the first mode $F_1(t)$ of the lateral Fourier decomposition at $z = 0$,

$$F(x,t) = F_0(t) + \mathrm{Re}\left[\sum_{n=1}^{\infty} F_n(t) e^{inkx}\right], \tag{4.4}$$

being the largest one suffices to characterize the evolution. For example, the initial linear growth dynamics can be described by the superposition,

$$F_1(t) \simeq A_L(t) e^{-i\omega_L t} + A_R(t) e^{-i\omega_R t}, \tag{4.5}$$

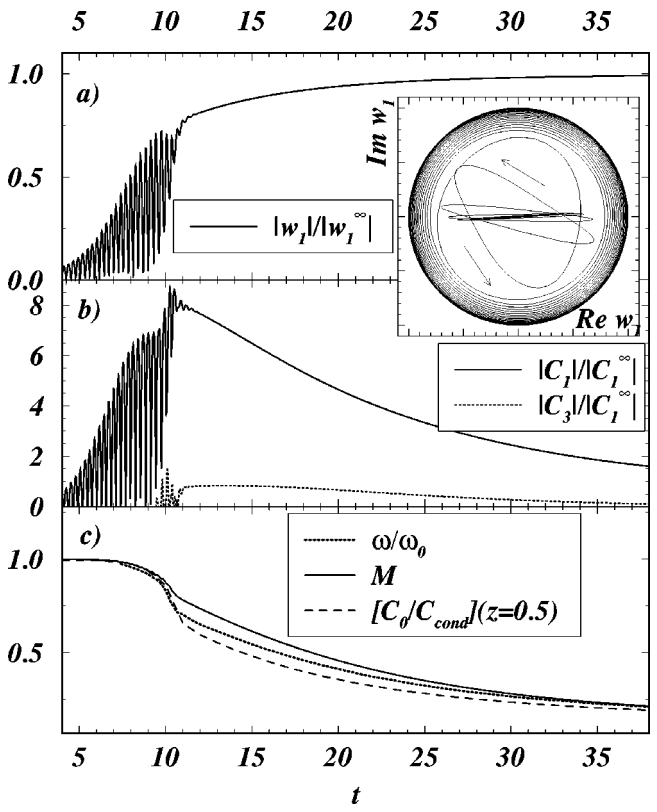

FIG. 4. (a),(b) Time evolution of lateral Fourier modes in the decomposition (4.4) of the fields at midheight of the fluid layer. The modulus $|w_1(t)|$ of the first mode of the vertical velocity field reduced by its final TW value $|w_1^\infty|$ is shown in (a). The inset shows the trajectory of $w_1(t)$ in the complex mode plane. In (b) we show $|C_1(t)/C_1^\infty|$ and $|C_3(t)/C_1^\infty|$. In (c) we show the frequency $\omega(t)$ reduced by the initial ω_0, the mixing number $M(t)$ [Eq. (2.4)], and the lateral average $C_0(z=0.5,t)$ of the concentration field at the upper plate reduced by its initial value $C_{cond}(z=0.5) = 0.125$ in the conductive state. The flow amplitudes $|A_{R,L}|$ of the two TWs of which the original SW is composed reach the respective phase velocites $\pm\omega/k$ (cf. Sec. IV E) roughly at the time 10. Parameters are $L = 0.01$, $\sigma = 10$, $\psi = -0.25$, $r = 1.42$, and $\lambda = 2$.

of a left and right propagating wave with amplitude moduli $|A_{L,R}| \propto e^{\gamma t}$ that grow with a common exponential rate γ. The latter and the oscillation frequencies $\omega_R = -\omega_L = \omega_0$ are initially given by the two complex conjugate eigenvalues that result from a linear stability analysis of the conductive state performed for $k = \pi$ at the slightly supercritical Rayleigh number $r = 1.42$ [29].

In Fig. 4(a) we show the time dependence of the modulus $|w_1(t)|$ of the first lateral Fourier mode of the vertical velocity field together with the trajectory of w_1 in the complex plane (inset of Fig. 4). The time evolution of $T_1(t)$ is very similar to the one of $w_1(t)$ and is, therefore, not shown here. Initially, one has $|A_L| \simeq |A_R|$, i.e., $\eta \simeq 0$ so that $w_1(t) \propto e^{\gamma t}\cos(\omega t)$ oscillates with growing amplitude along a straight line through the origin in the inset of Fig. 4. Thus, the modulus $|w_1(t)|$ becomes periodically very small — only when $|A_L| = |A_R|$, i.e., when $\eta = 0$ does $|w_1(t)|$ *exactly* touch zero. During this initial phase we have essentially SW dynamics, $w(x,t) \propto e^{\gamma t}\cos(\omega t)\cos(kx)$. However, with $|A_L|$

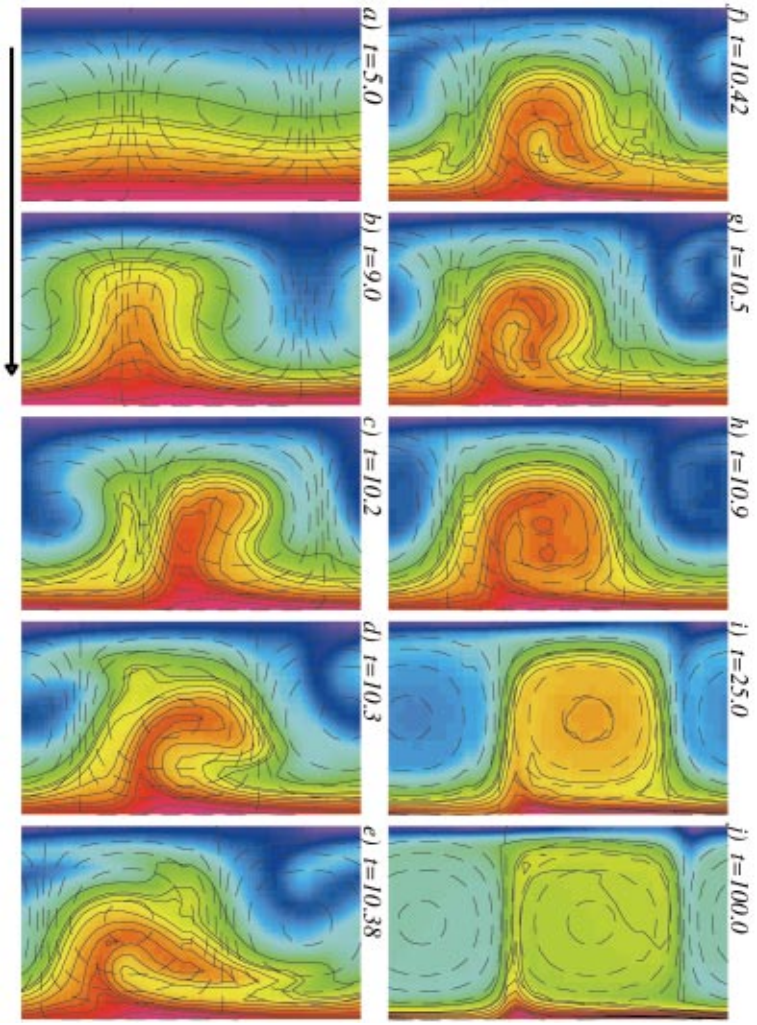

FIG. 5. (Color) Snapshots of the concentration redistribution in the SW→TW transformation. The concentration distribution in a vertical cross section of the fluid layer is displayed for one wavelength by color coded plots (with blue and red denoting high and low concentration, respectively) and by full isoconcentration lines (for $C>0$). Dashed lines are streamlines, i.e., tangents to the instantaneous velocity field. See text for a discussion of the plots (a)–(j). The final TW (j) propagates to the left. Parameters are $L=0.01$, $\sigma=10$, $\psi=-0.25$, $r=1.42$, and $\lambda=2$.

$\neq|A_R|$ the complex mode vector w_1 really traces out from the beginning on an ellipse in the inset of Fig. 4, albeit a narrow one. The associated phase winding behavior causes the pattern to be translated.

Then, the complex mode vector w_1 traces out a trajectory in the complex plane of the inset of Fig. 4 that becomes more and more circular. This behavior starts at about $t=10$ and reflects the fact that $|A_L|$ continues to grow while $|A_R|$ starts to decrease during the SW→TW transformation phase. Therein the nonlinear interaction between the two counterpropagating TWs that the original SW is made of causes the initially larger amplitude $|A_L|$ to win the competition that is well known from coupled complex amplitude equations [2]. As a result the elliptic spiral in Fig. 4 transforms into an outwards moving circular spiral and the minima of $|w_1(t)|$ are no longer small but grow. After time $t\simeq 11$ we have $A_R \simeq 0$ and a pure TW: the complex mode vector $w_1(t) = |w_1(t)|e^{i\varphi_1(t)}$ is spiralling outwards with slowly growing radius $|w_1(t)|$ and slowly decreasing rotation rate $\omega(t) = \dot{\varphi}_1(t) = -\omega_L(t)$ that is shown in Fig. 4(c).

The most conspicuous difference between the behavior of w_1, T_1 on the one hand and of C_1 on the other hand is the enormous overshooting of $|C_1|$ in Fig. 4(b) by about of factor of 10 relative to the final TW value of $|C_1^\infty|$ during the interaction and transformation phase around $t=10$. In contrast to this behavior the SW→TW transformation for w and T is rather smooth and unspectacular with a monotonously growing amplitude of the left propagating w- and T wave. For the concentration wave, however, the SW→TW transformation is triggered by a breaking and toppling of the SW that is also accompanied by a strong growth of anharmonicity of the wave, i.e., of higher lateral Fourier modes of C – see, e.g., the dotted curve for $|C_3(t)/C_1^\infty|$ in Fig. 4(b). In the toppling and breaking concentration wave the coherence between the lateral Fourier modes of C is lost thus reflecting the complex, irregular redistribution (cf. Sec. IV C) that takes place in the short time interval of the SW→TW transformation. Thereafter a slow, long-time diffusive concentration relaxation takes place. This can be seen not only in Fig. 4(b) but also in Fig. 4(c). There we show the mixing number $M(t)$ (2.4), i.e., the concentration variance, the frequency $\omega(t)$, and the laterally averaged concentration at the upper plate $C_0(z=0.5,t)$, i.e., half of the total mean vertical concentration difference across the fluid layer. All these global characteristica of the concentration field — the common shape of the curves of ω, M, and $C_0(z=0.5)$ in Fig. 4(c) reflect the fact that these quantities are strongly tied together [10] also in transient processes — show a sharp drop at the end of the SW→TW interval.

C. SW→TW transformation

The SW→TW transformation amounts to a complex concentration redistribution that involves wave breaking and a competition phase where one of the TWs, of which originally the SW is composed, survives on cost of the other when nonlinear advection becomes sufficiently strong. The transformation being quite abrupt displays rather complex dynamics that is elucidated in more detail in this section. To that end we show in Fig. 5 a sequence of color coded sideview snapshots of the concentration distribution in the layer and of the instantaneous streamlines (dashed lines).

1. Concentration redistribution

Initially, at time $t=5$ in Fig. 5(a), we see the SW as it is typically found in the exponential growth phase. The dashed streamlines giving instantaneous tangential flow directions show how alcohol is transported upwards and downwards by the SW flow that reverts periodically its direction. The vertical concentration gradient is as large as that of the quiescent conductive state. The lateral one is still small so that here the lateral SW profile is still harmonic. At $t=9$ [Fig. 5(b)], however, the flow amplitude of the SW oscillation has already become so large that the upwards and downwards bulging concentration plumes reach the opposite top and bottom boundary, respectively. Beyond the midplane the streamlines diverge sideways, thereby widening the concentration wave and making it anharmonic. Advective nonlinearities have by now become sufficiently strong to amplify the mirror-symmetry-breaking differences between the original, left- and right-propagating TW constituents of the SW to a level such that they are clearly visible (in Sec. IV D we show that *perfectly* mirror-symmetric initial conditions evolve into *perfect* SW transients that under otherwise ideal conditions do not lose their mirror symmetry and that end up in an unstable, mirror-symmetric SOC state). The advective amplification of the mirror-symmetry-breaking causes, in particular, asymmetric deformations of the concentration plumes that can be seen upon close inspection already in Fig. 5(b) and more clearly so in Fig. 5(c).

This figure marks the start of the extremely fast, advection dominated wave breaking process that lasts only about 0.3 thermal diffusion times and that is documented for $10.2 \leqslant t \leqslant 10.5$ in Figs. 5(c)–5(g). Therein the flow bends the deformed red and blue plumes sideways to the right (c), folds them (d), and then in (e) the red one is pushed downwards and the blue one upwards. In (e) and (f) the relative position of the streamlines and of the concentration distribution has changed such that now the plume structure of the latter is partially resurrected by the flow. Simultaneously the plumes get ''rolled in.'' This flow induced sequence of first deforming, then bending, and finally rolling in the plumes is triggered and associated with a change of the *spatial* phase between velocity and concentration field as shown in Figs. 3 and 6. In the SW the spatial location of the nodes of C and w coincide while the oscillations of C and w are only temporally shifted by about a quarter of an oscillation period, i.e., $\Delta t \simeq 0.14$. This phase difference $\varphi_C - \varphi_w \simeq \pi/2$ does not change its value but in the TW it implies also a spatial difference of about $\lambda/4$ between the TWs of C and w.

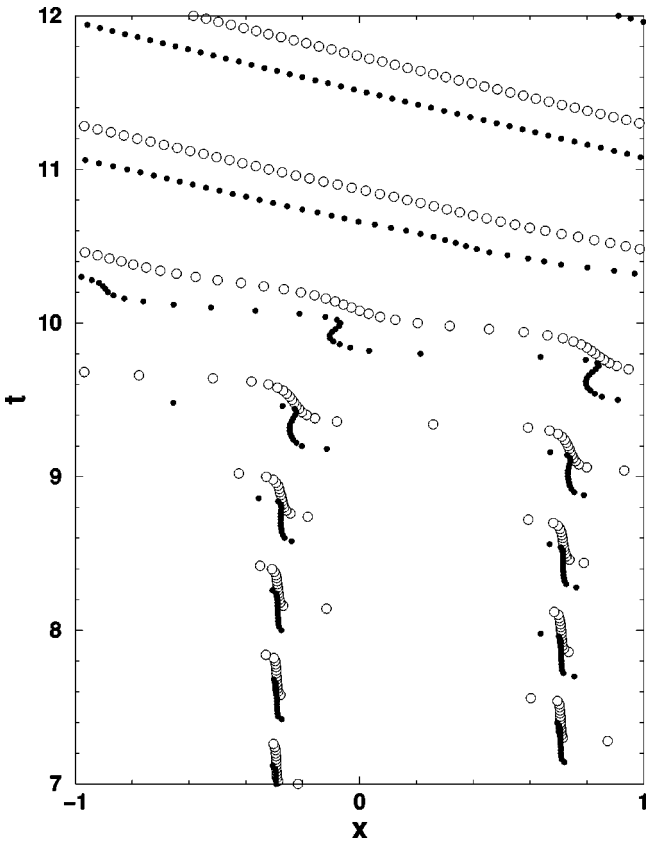

FIG. 6. Spatiotemporal evolution of the phases of the waves of vertical velocity w and concentration C during the SW→TW transformation. Shown are the world lines of the nodes of w (open circles) and C (filled circles) with positive slope at midheight of the layer. The half-wavelength jumps of the SW nodes (lower part of the figure) of w are temporally delayed by about a quarter oscillation period relative to those of C. While the frequency of the waves decreases slightly [cf. Fig. 4(c)] the value of the phase shift, $\varphi_c - \varphi_w \simeq \pi/2$, does not change. It implies also a spatial delay of about $\lambda/4$ between the TWs of w and C in the upper part of the figure. Parameters are $L=0.01$, $\sigma=10$, $\psi=-0.25$, $r=1.42$, and $\lambda=2$.

The advective process (f) and (g) of rolling the plumes into the circular regions of closed streamlines produces characteristic concentration striations that can still be seen in (g) and (h). The latter are the first snapshots of the emerging TW that has still the large concentration gradients of the conductive state so that, therefore, its propagation velocity ω/k is almost as fast as the Hopf phase velocity ω_H/k. Thereafter the rolled-in striations are degraded and homogenized by slow diffusion leading to a slowing down of the TW until finally, in (j), the fluid is well mixed to the level of the slow final-state TW.

A comparison of Fig. 5 with Fig. 4 revealing further insight is instructive: The nonlinear advective deformation of the SW concentration plumes in Fig. 5 starts when in Fig. 4 the modulus oscillations of the lateral harmonics $|w_1|$ and $|C_1|$ do no longer go down to zero, that is, when the straight-line SW trace of $w_1(t)$ in the inset of Fig. 4 develops a sizeable elliptic shape that reflects the growth of the left-

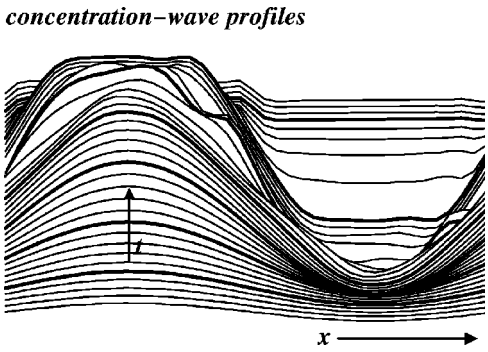

FIG. 7. Time evolution of the lateral profiles of the concentration field at midheight as a hidden-line plot. The profiles of the initial SW are taken when their amplitude is maximal, the TW propagation is compensated. Thick lines show profiles at (nonequidistantly spaced) times $t=4.56$, 5.92, 7.3, 8.74, 11.84, 20.28, 70.04. Lines behind the crests on the left appear on the right as troughs because of the mirror-glide symmetry. Parameters are $L=0.01$, $\sigma=10$, $\psi=-0.25$, $r=1.42$, and $\lambda=2$.

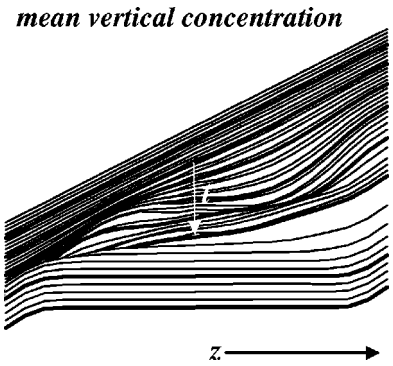

FIG. 8. Time evolution of the vertical profiles of the laterally averaged concentration field $C_0(z)$ as a hidden-line plot. Thick lines show profiles at (nonequidistantly spaced) times $t=4.56$, 5.92, 7.3, 8.74, 11.84, 20.28, 70.04. Parameters are $L=0.01$, $\sigma=10$, $\psi=-0.25$, $r=1.42$, and $\lambda=2$.

propagating TW on cost of the right-propagating component in the original SW. Thus, the competition of the two counterpropagating TWs is related to the boundary-induced deformation and the subsequent toppling of concentration plumes caused by a change in the spatial phase relation between velocity and concentration wave, cf., Figs. 3 and 6.

The toppling, bending, and rolling in of the SW concentration plumes is also reflected by and associated with a complicated time dependence of the higher lateral concentration modes – see, e.g., $|C_3(t)|$ in Fig. 4(b) around $t\simeq 10$. Higher C modes are here excited as well with complicated, incoherent phase relations relative to each other in the SW→TW transformation phase.

The moduli $|C_n(t)|$ become slowly varying only after the pure TW has emerged out of the breaking process, say, after $t\simeq 11$. Then, in the relaxing TW, the phase relations between the lateral Fourier modes are locked in, their phase velocities are multiples of the frequency $\omega(t)$ of the first harmonic shown in Fig. 4(c), and they all decrease with decreasing concentration variance $M(t)$ [Fig. 4(c)]. The decrease of ω and M is correlated also with a decrease of the mean vertical concentration difference between the surplus $C_0(z=0.5)$ at the top plate and the deficiency, $C_0(z=-0.5)=-C_0(z=0.5)$, at the bottom plate as can be seen from the dashed line in Fig. 4(c).

2. Evolution of concentration profiles

Lateral as well as vertical profiles of the concentration wave change significantly during the SW→TW transformation as it can already be seen in Figs. 3 and 5 and in more detail in Figs. 7 and 8. In Fig. 7 we show the temporal evolution of the concentration deviation from its mean at midheight, $C(x,z=0)$, by hidden-line plots at various times increasing from bottom to top. First the profile of the small-amplitude SW is harmonic and remains so while the amplitude grows, then there appear anharmonicities in the bending and rolling-in process, and, thereafter, the trapezoidal profile of a TW emerges with its characteristic plateaus at constant concentration deviation of opposite sign. In the subsequent evolutionary phase with slow relaxation towards the final-state TW the lateral extension of the plateaus increases while their height decreases dramatically.

In Fig. 8 we show the temporal evolution of the vertical profile of the laterally averaged concentration distribution $C_0(z)$ by hidden-line plots at various times increasing from top to bottom. The top line is the linear conductive profile with its large gradient and large surplus (deficiency) of concentration at $z=0.5$ (-0.5). The bottom line is the mean vertical concentration profile of the almost relaxed TW at $t=70.4$. It is characterized by a vanishing of C_0 over most of the fluid layer (cf. the broad plateau in Fig. 8). Furthermore, the final TW has quite narrow top and bottom boundary layers and the concentration surplus (deficiency) at the top (bottom) boundary is much smaller than in the conductive state or in the early SW. These properties again reflect the fact that the slowly propagating final TW is a well mixed state. During the SW→TW tranformation phase there appear undulations on the initially linear profiles that then flatten out in the bulk to the $C_0=0$ plateaus. Simultaneously the concentration $C_0(z=0.5)=-C_0(z=-0.5)$ at the boundaries is reduced considerably to the final TW levels as it can also be seen from the dashed curve in Fig. 4(c).

D. Initial state dependence

The transient growth behavior displays a peculiar sensitive dependence on the initial state that is absent in the growth of convection in pure fluids. Therein, only one critical mode can grow out of the conductive state after disturbing it with some unspecified small perturbation. The resulting supercritical growth dynamics of pure fluid convection shows an exponential growth phase determined by the critical mode, a saturation phase, and finally the relaxation into the fixed point of the final state of SOC. The transients resulting from different generic perturbations that contain the critical pure-fluid mode with different amplitude are the same after shifting them in time if one disregards the very early times that just reflect the respective perturbation dy-

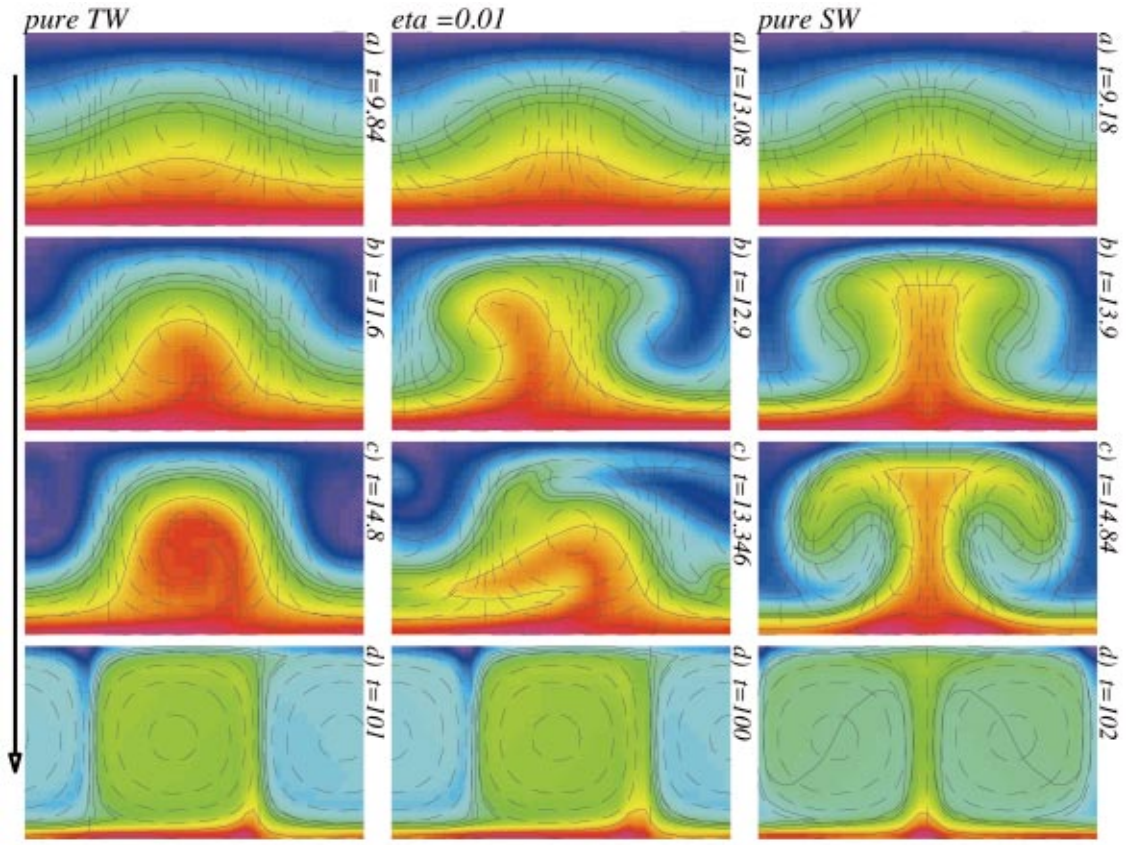

FIG. 9. (Color) Dependence of the transient convective growth behavior on the amplitudes $|A_{R,L}|$ of $\mathcal{TW}_{R,L}$ modes contained in the initial perturbation of the conductive state. The relative amplitudes η (4.3) are 1 in the first row (pure TW), 0.01, and 0 in the third row (pure SW). Snapshots of instantaneous streamlines (dashed) and color coded concentration distributions (blue and red denotes high and low concentration, respectively) together with isoconcentration lines (full) are shown over one wavelength in a vertical cross section of the layer. Times increase from top to bottom and are chosen to display characteristic field configurations for the respective evolution scenario. Parameters are $L=0.01$, $\sigma=10$, $\psi=-0.25$, $r=1.42$, and $\lambda=2$.

namics. The reason is that after these very early times the transients are governed and slaved by just one growing mode.

In binary mixture convection with negative Soret coupling, however, there are two critical modes, $\mathcal{TW}_R(x,z,t)$ and $\mathcal{TW}_L(x,z,t)$ of right and left propagating TW perturbations [32,54,56], respectively, that get involved. They are mutual mirror images with respect to the symmetry operation $x\rightarrow -x$ and they both grow above the Hopf bifurcation threshold with the same growth rate as long as linear theory applies. In a generic initial perturbation of the conductive state these two critical modes will be contained with different nonzero amplitudes A_R and A_L. Perturbations with $|A_R|=|A_L|, A_R=0$, or $A_L=0$ are nongeneric special cases with significantly different transient growth behavior than the generic case.

We found that the transients can be characterized by the relative amplitude difference η [Eq. (4.3)] of the two critical TW modes contained in the initial perturbation. Their relative strength determines the competition of these two waves when the advective nonlinearities become important. Figures 9 and 10 elucidate the dependence of the transient behavior on the relative content of $\mathcal{TW}_R$ and of $\mathcal{TW}_L$ for the special case of a pure right-propagating TW perturbation ($\eta=1$), a mixed perturbation with $\eta=0.01$, and a pure SW perturbation ($\eta=0$). The perturbation with $\eta=1$ has been imposed to contain only the critical $\mathcal{TW}_R$ mode. In the case of $\eta=0$ the numerically determined $\mathcal{TW}_R$ and $\mathcal{TW}_L$ critical modes [57] for the fields u,w,T,C were superimposed with exactly equal amplitude to form a perfectly mirror-symmetric initial state. Since our finite-difference integration code was constructed [58] not to generate mirror-symmetry breaking round off errors all fields remained mirror symmetric for all times in the case $\eta=1$.

Generic initial perturbations of the conductive state, on the other hand, were generated by 800 uniformly distributed pseudorandom numbers in the range of $[-10^{-4},10^{-4}]$ added to the conductive temperature field on the grid of the simulation. In this way we found that $|\eta|$ is generically nonzero but small compared to 1. This reflects the fact that the mirror symmetry under $x\rightarrow -x$ is only weakly broken when constructing the initial perturbation in the above described generic way. This also explains that one observes in experiments initially a growth phase with SW characteristics when the set up and with it the perturbations of the conductive state are almost mirror symmetric so that a particular TW propagation direction is not favored [16].

Figure 9 shows instantaneous streamlines (dashed) and color coded concentration distributions together with isocon-

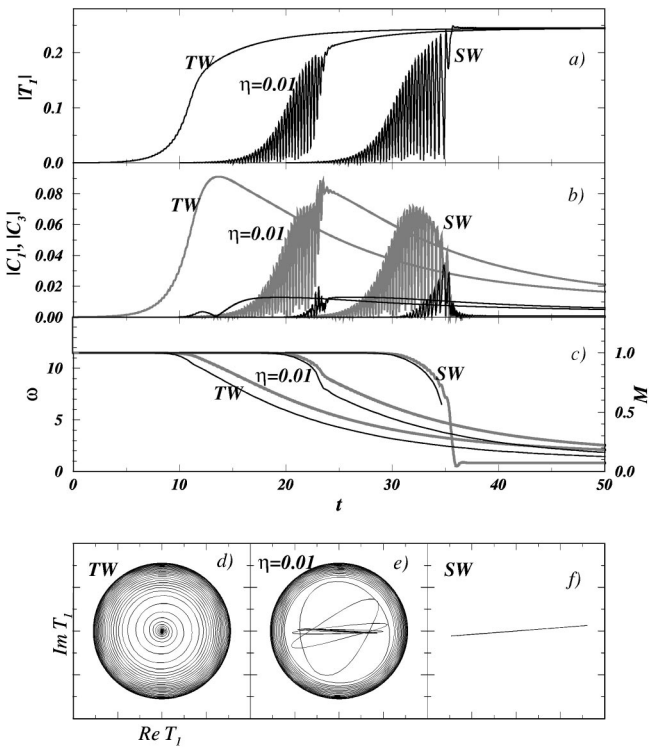

FIG. 10. Evolution dynamics of the moduli of lateral Fourier modes at midheight of the layer as indicated, of the frequency ω, and of the mixing number M for the three transition scenarios of Fig. 9 with $\eta=1$ (pure TW), $\eta=0.01$, and $\eta=0$ (pure SW). The starting times for the three scenarios have been shifted by $\Delta t=10$ relative to each other for better visibility. The last row shows the dynamics in the complex mode plane of T_1 (the velocity mode w_1 behaving similarly). Parameters are $L=0.01$, $\sigma=10$, $\psi=-0.25$, $r=1.42$, and $\lambda=2$.

centration lines (full) in a vertical cross section of the layer at four times. The latter were chosen differently for each of the three evolution scenarios such as to display field configurations that are characteristic for the respective evolution scenario. The first row of Fig. 9 shows an evolution stage where the noncritical modes that the initial perturbation might have contained have already died out but where the nonlinearities have not yet become important. Here the fields, say, at midheight of the layer are well described according to Eqs. (4.4) and (4.5) by $F=F_0+|A_R|\cos(kx-\omega t-\varphi_F)+|A_L|\cos(kx+\omega t+\varphi_F)$ since $A_{R,L}=|A_{R,L}|e^{\mp i\varphi_F}$ and $\omega_{R,L}=\pm\omega$. In the three cases of a pure right-propagating TW ($|A_L|=0$), a superposition of $\mathcal{T}W_R$ and $\mathcal{T}W_L$ with $\eta=0.01$, and a perfectly mirror-symmetric SW ($|A_R|=|A_L|$) the spatial separation between the nodes of the velocity and concentration fields are different because of the different amplitudes.

In the second row the nonlinearities have generated sizeable higher modes that are different for the three cases shown in Fig. 9. The spatial phase difference between velocity and concentration field has already slightly changed in the case $\eta=0.01$.

The next row shows for the pure TW evolution scenario ($\eta=1$) how the concentration bulges that intrude from the boundaries into the bulk of the fluid are rolled in to form later on patches with alternatingly high and low concentration plateaus. The generic case, $\eta=0.01$, shows in the third row the wave toppling occuring in the transition (Sec. IV C) to a genuine TW. In the perfectly symmetric case of $\eta=0$ advection has become strong enough to deform the SW concentration distribution into the shape of a symmetric mushroom just before there occurs an abrupt lock-in transition to a stationary field configuration. This sudden locking in of the mushroomlike configuration terminates the SW oscillations. Thereafter a very fast relaxation to the mirror-symmetric final-state SOC takes place that is dominated by advective mixing. The SOC and the previous SW transients are unstable against mirror-symmetry-breaking perturbations that would drive the system to one of the stable nonlinear TW states. However, by carefully avoiding these perturbations in our code we can trace out the pure SW transition scenario all the way to the final unstable SOC. Here it should be noted that for our control parameters neither a stable nor an unstable nontransient, relaxed SW solution is available: The nonlinear, unstable SW solution branch bifurcates backwards out of the conductive state at Hopf bifurcation threshold r_{osc}, ends on the lower unstable SOC solution branch, and remains always below r_{osc} [10,59].

The last row in Fig. 9 shows the final states of the respective evolution: the nonlinear TW state for $\eta=1$ and $\eta=0.01$ and the SOC state for the perfectly symmetric SW ($\eta=0$).

In Fig. 10 we show the dynamics of the lateral Fourier modes T_1, C_1, and C_3 at midheight of the fluid layer, of the frequency ω, and of the mixing number M for the three cases of Fig. 9. The starting times for the three curves have been shifted in Figs. 10(a)–10(c) relative to each other for better visibility.

The initial condition $\eta=1$ with a pure right propagating TW perturbation leads to an outwards spiraling motion of T_1 in the complex mode plane of Fig. 10(d) with monotonously increasing $|T_1|$ and $|w_1|$ [Fig. 10(a)]. On the other hand, $|C_1|$ develops a strong overshoot in Fig. 10(b) when the concentration bulge in the third row of Fig. 9 is rolled in. Thereafter, there is a long-time diffusive relaxation of $|C_1|$ as well as of M and ω in Fig. 10(c). The transition of the fast TW to the long-time relaxation phase is associated with the appearance of higher lateral Fourier modes, e.g., $|C_3|$ in Fig. 10(b).

The other nongeneric case, $\eta=0$, triggered by a perfectly symmetric SW initial perturbation shows oscillatory motion of T_1 along the straight line in Fig. 10(f) until the SW abruptly stops—cf. the termination of the curve for ω in Fig. 10(c)—and is locked into a stationary field configuration. The latter almost instantaneously evolves into the SOC, cf. the evolution of M in Fig. 10(c). Also here the transition is associated with the generation of higher lateral Fourier modes of the concentration field some of which surpass in magnitude even the first mode.

The evolution of the Fourier modes, of ω, and of M for the generic case $|\eta|=0.01$ that has been dicussed at length in Secs. IV A–IV C is included here in Fig. 10 for the sake of better comparison with the nongeneric cases. We only mention that the long-time diffusive transients for $\eta=1$ and $\eta=0.01$ are the same.

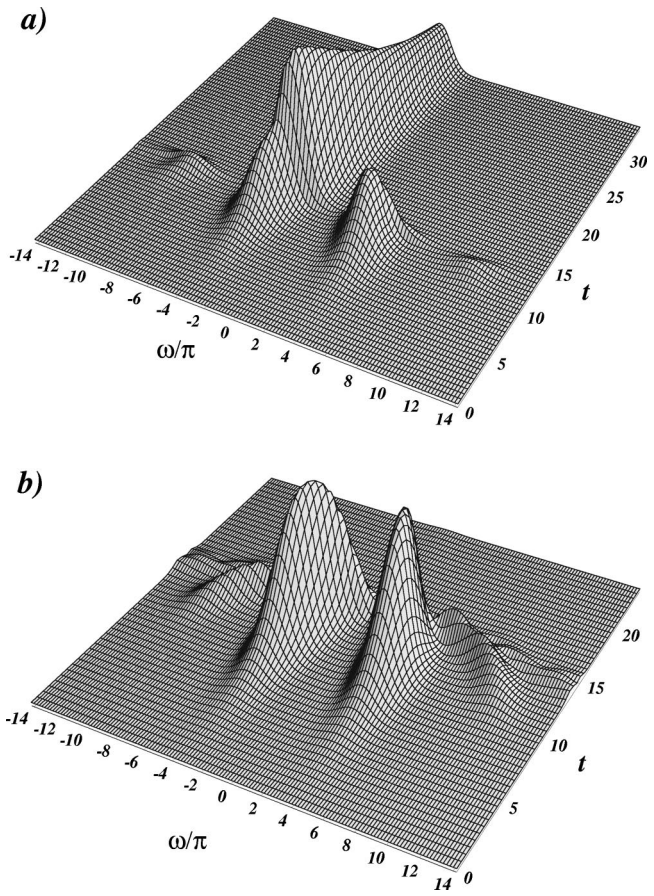

FIG. 11. Time evolution of the frequency spectrum $|C_1(\omega;t)|$ obtained as the Fourier transform with a Gaussian window centered at time t of the first lateral concentration mode at midheight of the layer. In the generic growth scenario (a) the initial perturbation contained the right and left propagating critical modes $TW_{R,L}$ with relative weight $\eta(4.3)=-0.01$. In the pure SW scenario (b) $\eta=0$. Parameters are $L=0.01$, $\sigma=10$, $\psi=-0.25$, $r=1.42$, and $\lambda=2$.

E. Competition between right and left propagating TWs

Here we analyze the competition between the growing right- and left-propagating TW with the help of the complex signal $F_1(t)$ of the first lateral Fourier mode of different fields at midheight of the layer. Since the frequency, i.e., the rate of change of the phase of F_1 varies considerably we made a spectral analysis of F_1 that is local in time by multiplying $F_1(t)$ with a Gaussian window whose center is gliding along the time axis. The window width was adjusted to get good resolution without too much overlap of the spectra centered at the TW frequencies $\omega_R(t)$ and $\omega_L(t)=-\omega_R(t)$, respectively. As an aside we mention that the method [60] of shifting the whole signal in frequency space and applying a low-pass filter to extract the wave in question could not be applied in our case because of the strong temporal variation of the wave frequencies.

Figure 11 shows the time evolution of $|C_1(\omega;t)|$ where $C_1(\omega;t)$ is the Fourier transform of the time signal C_1 evaluated with a Gaussian window centered at time t. Here the initial state contained the right and left propagating critical modes $TW_{R,L}$ with relative amplitude difference $\eta=-0.01$ [Fig. 11(a)] and $\eta=0$ [Fig. 11(b)], respectively. The Gaussian shaped contribution from the right- (left-) propagating TW is centered at positive (negative) frequencies. Initially both grow exponentially and independently from each other in agreement with linear theory. But when the convective nonlinearities have become sufficiently strong the two waves begin to compete. It leads in the case of $\eta=-0.01$ to a rapid decay of the right-propagating minor wave and an enhanced growth of the left-propagating major wave. The latter continues to grow in amplitude before the long-time diffusive relaxation to the final low frequency, low amplitude, well mixed nonlinear TW state begins. In this relaxation phase the crest of the mountain ridge in Fig. 11(a) decreases in height and moves towards 0.

In the perfectly symmetric SW scenario [Fig. 11(b)] the competition between the counterpropagating waves with precisely equal amplitudes ($\eta=0$) leads to an extinction of the waves and a lock-in transition to a stationary state. However, the stationary C_1 mode in the final SOC state is too small [cf. Fig. 10(b)] to be resolved in Fig. 11—the uncertainty relation does not allow to trace the frequencies down zero. In both cases shown in Fig. 11 there appear higher-frequency harmonics in $C_1(t)$ during the interaction and competition phase. But because of the mirror-glide symmetry of $C(x,z,t)$ they appear at midheight, $z=0$, only for odd multiples of the basic frequency of $C_1(t)$. The magnitude of these higher harmonics increases with decreasing $|\eta|$, i.e., when the amplitudes of the counterpropagating TWs become more and more equal.

In Fig. 12 we show the time evolution of the TW amplitudes in the plane spanned by $|A_R|$ and $|A_L|$ for various initial conditions with different η. These amplitudes were taken from the frequency decomposition of the windowed Fourier transformation of $w_1(t)$ since the vertical velocity field remains practically harmonic. Thus, the representation of the whole w field by $w_1(t)$ is much better than the one of C by $C_1(t)$. The resulting symbols in Fig. 12 are plotted at equidistantly spaced times to indicate the velocities with which different parts of the trajectories are traced out. They connect the small initial perturbation of the unstable conductive state fixed point ($A_{R,L}=0$) to the two TW attractors when $\eta\neq 0$ or to the unstable SOC fixed point when $\eta=0$.

Trajectories starting from initial conditions with $\eta=\pm 1$ move straight to the two TW attractors along the axes in Fig. 12. On the other hand, the trajectory originating from the pure SW initial condition, $\eta=0$, moves in Fig. 12 to the unstable SOC fixed point along the diagonal that connects the unstable conductive state fixed point with the unstable SOC state. All trajectories with $\eta\neq 0$ merge with—or, to be more precise, approach—the pure TW trajectories along the abscissas before ultimately ending in one of the TW attractors. But the closer η is to 0 the longer stays the respective trajectory close to the diagonal before it is eventually attracted to one of the TW attractors. Thus, the diagonal is a separatrix, i.e., a boundary between the basins of attraction of the two TW attractors—trajectories starting from initial conditions with $\eta<0$ ($\eta>0$) get attracted to the TW attractor on the ordinate (abcissa).

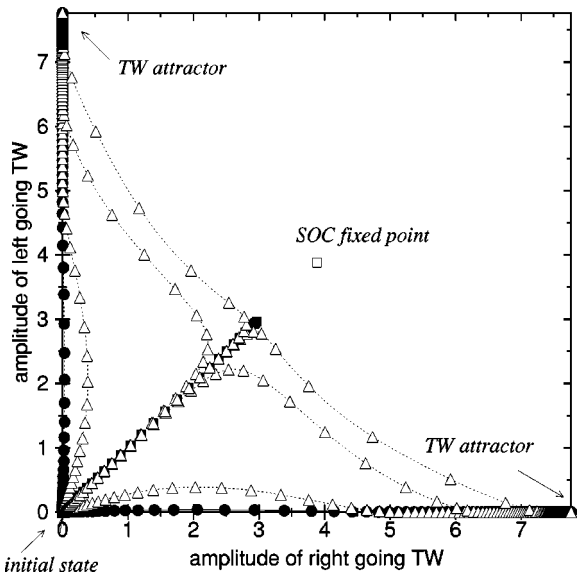

FIG. 12. Time evolution of TW amplitudes for initial conditions with different η. The amplitudes (symbols) of the respective TWs were determined at equidistantly spaced times by a frequency decomposition of the Fourier transformation of the first lateral harmonic, $w_1(z=0,t)$, of the vertical velocity field using a gliding time window described in the text. Parameters are $L=0.01$, $\sigma=10$, $\psi=-0.25$, $r=1.42$, and $\lambda=2$.

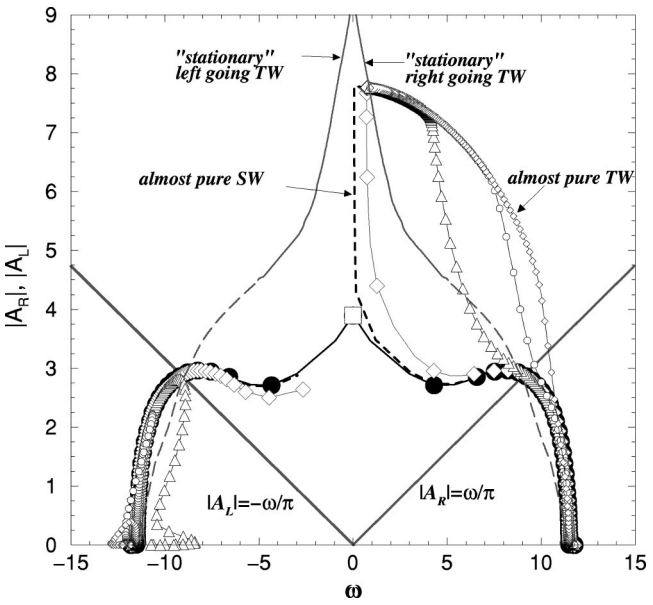

FIG. 13. Evolution trajectories in the plane spanned by frequency ω and TW flow amplitudes obtained from the Fourier decomposition of the first lateral harmonic, $w_1(z=0,t)$, of the vertical velocity field using a gliding time window as in Fig. 12. $|A_R|$ and $\omega>0$ ($|A_L|$ and $\omega<0$) refer to right- (left-) propagating TW contributions to w_1. Symbols are plotted at equidistantly spaced times starting on the abscissa ($|A_{R,L}|\simeq 0$, $\omega=\pm\omega_0\simeq\pm 11.5$) from small perturbations of the conductive state with $\eta=0$ [full lines with filled circles; these pure SW trajectories end in the unstable SOC state (open square)], 10^{-7} (dashed lines marked ''almost pure SW''), 10^{-6} (large open lozenges), 10^{-4} (open triangles), 10^{-2} (small open circles), 0.7 (small open lozenges marked ''almost pure TW''). The bifurcation branches of the nonlinear ''stationary'' stable and unstable TW solutions are included by full and dashed gray lines, respectively. The significance of the straight grey lines labeled $|A_{R,L}|=\pm\omega/\pi$ is explained in the text. Parameters are $L=0.01$, $\sigma=10$, $\psi=-0.25$, $r=1.42$, and $\lambda=2$.

There is a ''separation point'' on the diagonal connection between the two unstable fixed points in Fig. 12 from which trajectories with $\eta\neq 0$ are repelled and deflected towards one of the TW attractors. Pure SW trajectories, however, experience beyond this point an extremely large acceleration towards the SOC fixed point—see also Figs. 10 and 11. The special role that the separation point plays can be understood with the help of Fig. 13. There, we show trajectories starting from initial conditions with $\eta\geqslant 0$ (those with $\eta<0$ are just mirror images of the respective ones with $\eta>0$) in the plane spanned by frequency ω and moduli $|A_R|$ and $|A_L|$. Positive (negative) frequencies and amplitudes $|A_R|$ ($|A_L|$) refer to right- (left-) propagating TW contributions to $w_1(t)$ as obtained from the windowed Fourier transformation. The starting points $|A_{R,L}|\simeq 0$ on the absissa at $\omega=\pm\omega_0\simeq 11.5$ are small perturbations of the conductive state. For $\eta>0$ ($\eta<0$) the right- (left-) propagating TW contribution wins the competition and the trajectory of $|A_R|$ ($|A_L|$) ends on the bifurcation branch [12,48] of nonlinear, right (left) propagating ''stationary'' TWs that is included in Fig. 13 as well. The losing trajectory of $|A_L|$ ($|A_R|$), on the other hand, runs more or less abruptly (cf. also Fig. 11) back to the abscissa $|A|=0$. For perfect SW initial conditions with $\eta=0$, however, the ''pure SW'' trajectories in Fig. 13 end in the SOC state at $\omega=0$ tracing out the perfectly symmetric SW scenario with $|A_R|=|A_L|$.

All winning trajectories starting from initial conditions with $\eta\neq 0$ enter eventually the pure TW evolution phase—the sooner the closer $|\eta|$ is to 1 (which can also be seen in Fig. 12). The pure $\eta=1$ TW evolution trajectory is practically identical with the small open lozenges (labeled ''almost pure TW'') in the right part of Fig. 13. The pure TW evolution trajectories ($\eta=\pm 1$) trace out an ellipse given by the relation [29] $(\omega/\omega_0)^2+|A/A_\infty|^2=1$ between frequency and velocity field intensity. If $|\eta|$ is close to 1 as for the small open lozenges and circles the minor amplitude ($|A_L|$ in Fig. 13) becomes suppressed early during the competition. While the frequency ω_R of the winning TW decreases monotonously the frequency $|\omega_L|$ of the losing TW varies slightly around ω_0.

In the generic growth scenario that starts from perturbations with some finite $0\leqslant|\eta|\ll 1$ the trajectories remain in Fig. 13 initially close together since during the first growth phase the frequency ω does not deviate much from the initial Hopf frequency ω_0 (cf. Figs. 4 and 10). But when the flow intensities $|A_{R,L}|$ of the right- and left-propagating TW constituents reach the respective phase velocities $\pm\omega/\pi$, which happens near the separation point, then the evolution changes: The trajectories of the w-field in Fig. 13 undergo characteristic changes depending on η when they cross the lines $|A_{R,L}|=\pm\omega/\pi$ in Fig. 13 (while in Fig. 12 they get deflected towards the TW attractor). With decreasing $|\eta|$ they get more and more bent towards $\omega=0$, the axis of Fig. 13 (the absissa or ordinate in Fig. 12). But finally they

change direction to merge with the pure TW ellipse, $(\omega/\omega_0)^2+|A/A_\infty|^2=1$ in Fig. 13 (with one of the axes in Fig. 12). This happens with decreasing $|\eta|$ at later and later times.

This change in the dynamics close to the separation point is associated with the concentration redistribution that occurs when the fast initial SW-like oscillations of the generic case ($|A_R|\simeq|A_L|$, i.e., small $|\eta|\neq 0$) are transformed into TW oscillations (cf. Secs. IV A and IV C). This takes roughly place when the convective flow velocities $|A_{R,L}|$ have reached the respective phase velocities $\pm\omega/\pi$. Then the concentration wave crests and troughs topple; concentration is ''rolled in'' into regions with alternatingly high and low, plateaulike levels that are subsequently degraded diffusively on longer time scales as described in the previous subsections.

V. CONCLUSION

The spatiotemporal evolution of oscillatory convective roll structures during the transient growth out of perturbations of the quiescent conductive ground state has been investigated with finite difference numerical simulations of a laterally periodic fluid layer. To elucidate the spatiotemporal changes in the different transient growth scenarios we have studied the evolution of various field quantities like, e.g., computed topview shadowgraph intensity profiles, lateral Fourier modes (and their temporally windowed frequency spectra) of the fields and their trajectories in different phase spaces, sideview field distributions, lateral and vertical wave profiles, frequency and mixing number.

The simulations have been performed for parameters adapted to experiments that use ethanol-water mixtures with sufficiently negative Soret coupling to show a subcritical Hopf bifurcation. Then two critical modes of right- (R) and left- (L) propagating TWs with typically large positive and negative frequency, respectively, can grow above the Hopf bifurcation threshold. Thus, the transients show—unlike pure fluid convection—a peculiar sensitive dependence on the initial state. However, all transients investigated here obeyed the mirror-glide (MG) symmetry (3.1) with the exception of the very early stage when the imposed initial conditions were not MG symmetric. But, even then the MG symmetry was rapidly restored. The robustness of this symmetry is remarkable given that the nonlinearity in the concentration balance, i.e., the Péclet number w/L becomes large. However, the concentration field is ''tamed'' by being coupled to the MG symmetric velocity and temperature fields that in the investigated range of small supercritical driving remain smooth.

We found that the different growth scenarios can conveniently be characterized by the relative amplitude difference η [Eq. (4.3)] of the two critical TW modes contained in the initial perturbation of the conductive state. Their relative strength (which can easily be determined by Fourier decomposition) determines the outcome of the competition of these two waves when the advective nonlinearities become important. For *generic*, i.e., nonspecific initial perturbations that break the mirror symmetry $x\rightarrow -x$ only weakly one has $|A_R|\simeq|A_L|$ so that $|\eta|$ is small compared to 1 but nonzero. Thus, ''almost'' mirror-symmetric experimental setups that do not favor a particular TW propagation direction cause an initial growth phase with SW characteristics. On the other hand, the *pure* SW case $|A_R|=|A_L|$ and the two *pure* TW cases $A_L=0$ or $A_R=0$ with $\eta=\pm 1$ are nongeneric with significantly different transient growth behavior.

In the perfectly mirror-symmetric *pure* SW growth scenario ($\eta=0$) the SW oscillations terminate *abruptly* once they have reached a critical amplitude by locking in into the stationary field configuration of a nonlinear mirror-symmetric SOC state. However, this *pure* SW growth scenario is unstable against mirror-symmetry-breaking perturbations that cause propagation of the growing pattern to the right (left) if $\eta>0$ ($\eta<0$). Also for larger Rayleigh numbers where only the SOC attractor but no more steady TW solution is available as nonlinear final state do the transients typically show TW competition and phase propagation that finally slows down. Pure TW growth ($|\eta|=1$) proceeds in the amplitude-frequency plane along an ellipse $[(\omega/\omega_0)^2+|A/A_\infty|^2=1]$ from the ground state perturbed by a pure TW critical mode all the way to the final, nonlinear TW state. All trajectories with $\eta\neq 0$ merge eventually into this pure TW evolution modus—the later the smaller $|\eta|$.

The *generic* growth dynamics is triggered from perturbations containing the two critical oscillatory modes with roughly equal amplitudes. Initially, i.e., as long as linear theory applies they both grow exponentially with the same growth rate thus causing SW-like oscillations with the large Hopf frequency. But a competition between the two TW constituents sets in when the advective nonlinearities have become sufficiently strong. They amplify the mirror-symmetry-breaking differences between $|A_R|$ and $|A_L|$ and cause the decay of the minority TW. Thus, the SW that still has a large frequency is transformed into a fast TW. This SW$\rightarrow$TW transformation being advection driven is spatiotemporally complicated, in particular, for the concentration field and it implies a dramatic redistribution of concentration by advective ''rolling in'' of concentration. It takes place within less than one vertical thermal diffusion time and it starts roughly when the flow amplitudes of the two constituent TWs have grown to about the phase velocity $|\omega|/k$: First concentration is advected upwards and downwards in the form of plumes by the growing SW-like flow that reverts periodically its direction; the vertical concentration gradient being still as large as that of the quiescent conductive state. The SW$\rightarrow$TW transformation is triggered by an advective wave breaking and wave toppling process of the crests and troughs of the concentration wave whereas the waves of w and T do not undergo substantial structural changes. Advective nonlinearities have by now become sufficiently strong to make the mirror-symmetry-breaking differences between the original, left- and right-propagating TW constituents of the SW clearly visible. When the concentration wave crests (troughs) with high (low) alcohol content bend and topple they are advectively ''rolled in.'' In the toppling and breaking concentration wave the coherence between the lateral Fourier modes of C is temporarily lost thus reflecting the complex, almost irregular redistribution dynamics that takes place in the short time interval of the SW$\rightarrow$TW transformation.

The flow induced sequence of first deforming, then bend-

ing, and finally rolling in the plume-like wave crests and valleys is associated with and driven by a growth of the *spatial* phase shift between velocity and concentration field from zero to about $\lambda/4$ during the SW→TW transformation: In the SW the spatial location of the nodes of C and w coincide while their oscillations are shifted in time by about a quarter of an oscillation period. The value, $\varphi_C - \varphi_w \simeq \pi/2$, of this phase difference does not change during the whole transition sequence but in the TW it implies also a spatial shift of C and w of $\lambda/4$.

Rolling the plumes into circular regions of closed streamlines produces alternatingly high and low concentration plateaus in the resulting *propagating* and strongly anharmonic C wave with some characteristic stripes (as an aside: the appearance of C-wave plateaus when flow and phase velocities become equal marks for ''stationary'' TW solutions a characteristic variation in the bifurcation branch that delimits the applicability of small-amplitude expansions). The lateral concentration difference between adjacent roll-like regions is in the early TW phase still almost as large as the initial vertical concentration contrast in the conductive state. Thus, frequency and phase velocity of this emerging TW is still very large, i.e., not much smaller than the critical values. But then a long-term TW transient to a low-frequency, strongly nonlinear, strongly anharmonic, relaxed TW state sets in: slow diffusion degrades and homogenizes the concentration striations, the spatial plateau extension over which C is constant at the two alternating high and low levels increases, the plateau height decreases, the width of boundary layers between these plateaus shrinks, the C-wave profile becomes more and more trapezoidal, and the alcohol surplus (deficiency) in the cold top (warm bottom) part of the fluid layer decreases, thereby reducing the overall vertical concentration difference between top and bottom. This long-time degradation of concentration gradients is reflected by a dramatic reduction of the mixing number M and with it of the frequency ω relative to the initial values—the better the fluid becomes mixed the smaller is ω.

ACKNOWLEDGMENTS

This work was supported by the Deutsche Forschungsgemeinschaft. Discussions with W. Barten and H. Schmitt and their contributions to an early stage of this research project are gratefully acknowledged. We thank R. Schmitz and M. Kamps for numerical support.

[1] A. Schlüter, D. Lortz, and F. Busse, J. Fluid Mech. **23**, 129 (1965).

[2] M. C. Cross and P. C. Hohenberg, Rev. Mod. Phys. **65**, 851 (1993), and references cited therein.

[3] For 5 w% of ethanol mixed into water at $T=20\,^{\circ}\mathrm{C}$ the separation ratio measuring the Soret coupling strength [2] is $\psi \simeq -0.3$ [61].

[4] For a review see [2,39]. Further references may be found, e.g., in [10,13]. See also the more recent publications [7,24–26,28,31,62] of some of the many groups that have investigated convection in binary mixtures.

[5] R. W. Walden, P. Kolodner, A. Passner, and C. M. Surko, Phys. Rev. Lett. **55**, 496 (1985).

[6] D. R. Ohlsen, S. Y. Yamamoto, C. M. Surko, and P. Kolodner, Phys. Rev. Lett. **65**, 1431 (1990).

[7] H. Touiri, J. K. Platten, and G. Chavepeyer, Eur. J. Mech. B/Fluids **15**, 241 (1996).

[8] W. Barten, M. Lücke, W. Hort, and M. Kamps, Phys. Rev. Lett. **63**, 376 (1989).

[9] D. Bensimon, A. Pumir, and B. I. Shraiman, J. Phys. (Paris) **50**, 3089 (1989).

[10] M. Lücke, W. Barten, P. Büchel, C. Fütterer, St. Hollinger, and Ch. Jung, in *Evolution of Structures in Dissipative Continuous Systems*, edited by F. H. Busse and S. C. Müller, Lecture Notes in Physics Vol. m55 (Springer, Berlin, 1998), p. 127.

[11] B. Shraiman, Phys. Rev. A **36**, 261 (1987).

[12] W. Barten, M. Lücke, and M. Kamps, Physica D **61**, 183 (1992).

[13] W. Barten, M. Lücke, M. Kamps, and R. Schmitz, Phys. Rev. E **51**, 5636 (1995).

[14] K. D. Eaton, D. R. Ohlsen, S. Y. Yamamoto, C. M. Surko, W. Barten, M. Lücke, M. Kamps, and P. Kolodner, Phys. Rev. A **43**, 7105 (1991).

[15] W. Barten, M. Lücke, and M. Kamps, in *Nonlinear Evolution of Spatio-Temporal Structures in Dissipative Continuous Systems*, Vol. 225 of *NATO Advanced Studies Institute, Series B: Physics*, edited by F. H. Busse and L. Kramer (Plenum, New York, 1990), p. 131.

[16] B. L. Winkler and P. Kolodner, J. Fluid Mech. **240**, 31 (1992).

[17] E. Moses and V. Steinberg, Phys. Rev. Lett. **60**, 2030 (1988); Physica D **37**, 341 (1989). See also the discussion [13,15,63] related to the interpretation of these results.

[18] P. Kolodner, A. Passner, C. M. Surko, and R. W. Walden, Phys. Rev. Lett. **56**, 2621 (1986); P. Kolodner, C. M. Surko, A. Passner, and H. L. Williams, Phys. Rev. A **36**, 2499 (1987); P. Kolodner and J. A. Glazier, *ibid.* **42**, 7504 (1990).

[19] C. M. Surko and P. Kolodner, Phys. Rev. Lett. **58**, 2055 (1987); V. Steinberg and E. Kaplan, in *Spontaneous Formation of Space-Time Structures and Criticality*, edited by T. Riste and D. Sherrington (Kluwer Academic Publishers, Amsterdam, 1991), p. 207.

[20] O. Lhost and J. K. Platten, Phys. Rev. A **38**, 3147 (1988); **40**, 4552 (1989).

[21] K. E. Anderson and R. P. Behringer, Physica D **51**, 444 (1991).

[22] P. Kolodner, C. M. Surko, and H. Williams, Physica D **37**, 319 (1989); J. Fineberg, E. Moses, and V. Steinberg, Phys. Rev. Lett. **61**, 838 (1988); P. Kolodner, *ibid.* **63**, 578 (1989); J. Fineberg, E. Moses, and V. Steinberg, *ibid.* **63**, 579 (1989).

[23] A. La Porta and C. M. Surko, Phys. Rev. E **53**, 5916 (1996).

[24] P. Kolodner, J. A. Glazier, and H. Williams, Phys. Rev. Lett. **65**, 1579 (1990); P. Kolodner, G. Flätgen, and I. G. Kevrekidis, *ibid.* **83**, 730 (1999).

[25] K. Lerman, E. Bodenschatz, D. S. Cannell, and G. Ahlers, Phys. Rev. Lett. **70**, 3572 (1993); K. Lerman, G. Ahlers, and D. S. Cannell, Phys. Rev. E **53**, R2041 (1996); K. Lerman, D.

S. Cannell, and G. Ahlers, *ibid.* **59**, 2975 (1999).
[26] C. M. Aegerter and C. M. Surko, Phys. Rev. E **63**, 046301 (2001).
[27] H. Schmitt, Diploma thesis, Universität des Saarlandes, Saarbrücken, 1992.
[28] L. Z. Ning, Y. Harada, and H. Yahata, Prog. Theor. Phys. **98**, 551 (1997).
[29] C. Fütterer, Ph.D. thesis, Universität des Saarlandes, Saarbrücken, 1999.
[30] P. Büchel and M. Lücke, Phys. Rev. E **61**, 3793 (2000); P. Büchel, Ph.D. thesis, Universität des Saarlandes, Saarbrücken, 1999.
[31] O. Batiste, M. Net, I. Mercader, and E. Knobloch, Phys. Rev. Lett. **86**, 2309 (2001).
[32] W. Schöpf and W. Zimmermann, Europhys. Lett. **8**, 41 (1989); Phys. Rev. A **41**, 1145 (1990); Phys. Rev. E **47**, 1739 (1993).
[33] T. Clune and E. Knobloch, Physica D **61**, 106 (1992).
[34] However, in Ref. [33] the small mean lateral flow generated by TWs [8,64] was explicitly incorporated. A large-scale concentration mode was introduced by H. Riecke, Phys. Rev. Lett. **68**, 301 (1992); Physica D **61**, 253 (1992) to model large-scale concentration redistributions of spatially localized TWs [49].
[35] G. W. Baxter, K. D. Eaton, and C. M. Surko, Phys. Rev. A **46**, R1735 (1992); P. Kolodner, *ibid.* **46,** R1739 (1992); P. Büchel and M. Lücke, Entropie **218**, 22 (1999).
[36] A. La Porta, K. D. Eaton, and C. M. Surko, Phys. Rev. E **53**, 570 (1996).
[37] G. Ahlers, Physica A **249**, 18 (1998).
[38] L. D. Landau and E. M. Lifschitz, *Hydrodynamik* (Akademie-Verlag, Berlin, 1966).
[39] J. K. Platten and J. C. Legros, *Convection in Liquids* (Springer, Berlin, 1984).
[40] W. Hort, S. J. Linz, and M. Lücke, Phys. Rev. A **45**, 3737 (1992).
[41] St. Hollinger and M. Lücke, Phys. Rev. E **52**, 642 (1995).
[42] J. L. Liu and G. Ahlers, Phys. Rev. Lett. **77**, 3126 (1996).
[43] G. W. T. Lee, P. Lucas, and A. Tyler, J. Fluid Mech. **135**, 235 (1983).
[44] J. E. Welch, F. H. Harlow, J. P. Shannon, and B. J. Daly, Los Alamos Scientific Laboratory Report No. LA-3425, 1966 (unpublished); C. W. Hirt, B. D. Nichols, and N. C. Romero, Los Alamos Scientific Laboratory Report No. LA-5852, 1975 (unpublished).
[45] R. Peyret and T. D. Taylor, *Computational Methods in Fluid Flow* (Springer, Berlin, 1983).
[46] Ch. Jung, Ph.D. thesis, Universität des Saarlandes, Saarbrücken, 1997.
[47] St. Hollinger and M. Lücke, Phys. Rev. E **57**, 4238 (1998).
[48] St. Hollinger, P. Büchel, and M. Lücke, Phys. Rev. Lett. **78**, 235 (1997).
[49] W. Barten, M. Lücke, and M. Kamps, Phys. Rev. Lett. **66**, 2621 (1991); W. Barten, M. Lücke, M. Kamps, and R. Schmitz, Phys. Rev. E **51**, 5662 (1995).
[50] Ch. Jung, B. Huke, and M. Lücke, Phys. Rev. Lett. **81**, 3651 (1998).
[51] A. Spina, J. Toomre, and E. Knobloch, Phys. Rev. E **57**, 524 (1998).
[52] St. Hollinger and M. Lücke, Z. Phys. B: Condens. Matter **103**, 531 (1997).
[53] V. Steinberg, G. Ahlers, and D. S. Cannell, Phys. Scr. **32**, 534 (1985); J. R. Jenkins, J. Fluid Mech. **190**, 451 (1988); S. Rasenat, G. Hartung, B. L. Winkler, and I. Rehberg, Exp. Fluids **7**, 412 (1989).
[54] W. Hort, Diploma thesis, Universität des Saarlandes, Saarbrücken, 1990.
[55] S. J. Linz and M. Lücke, in *Propagation In Systems Far From Equilibrium*, edited by J. E. Wesfreid, H. R. Brand, P. Manneville, G. Albinet, and N. Boccara (Springer, Berlin, 1988), p. 292.
[56] E. Knobloch and D. R. Moore, Phys. Rev. A **37**, 860 (1988); M. C. Cross and K. Kim, *ibid.* **37**, 3909 (1988).
[57] Ch. Jung (private communication).
[58] W. Barten, M. Lücke, and M. Kamps, J. Comp. Phys. **91**, 486 (1990).
[59] S. Hollinger, M. Lücke, and H. W. Müller, Phys. Rev. E **57**, 4250 (1998).
[60] P. Kolodner and H. Williams, in *Nonlinear Evolution of Spatio-Temporal Structures in Dissipative Continuous Systems*, Vol. 225 of *NATO Advanced Studies Institute, Series B: Physics*, edited by F. H. Busse and L. Kramer (Plenum, New York, 1990), p. 73.
[61] P. Kolodner, H. L. Williams, and C. Moe, J. Chem. Phys. **88**, 6512 (1988).
[62] E. Kaplan, E. Kuznetsov, and V. Steinberg, Phys. Rev. E **50**, 3712 (1994).
[63] M. Lücke, in *Far from Equilibrium Phase Transitions*, edited by L. Garrido (Springer, Berlin, 1988), p. 195.
[64] S. J. Linz, M. Lücke, H. W. Müller, and J. Niederländer, Phys. Rev. A **38**, 5727 (1988).